

UCLA

UCLA Electronic Theses and Dissertations

Title

Graphene Electronic Device Based Biosensors and Chemical Sensors

Permalink

<https://escholarship.org/uc/item/15441754>

Author

Jiang, Shan

Publication Date

2014

Peer reviewed|Thesis/dissertation

UNIVERSITY OF CALIFORNIA

Los Angeles

Graphene Electronic Device Based Biosensors and
Chemical Sensors

A dissertation submitted in partial satisfaction of the
requirements for the degree Doctor of Philosophy in
Chemistry

by

Shan Jiang

2014

© Copyright by

Shan Jiang

2014

ABSTRACT OF THE DISSERTATION

Graphene Electronic Device Based Biosensors and Chemical Sensors

by

Shan Jiang

Doctor of Philosophy in Chemistry

University of California, Los Angeles, 2014

Professor Xiangfeng Duan, Chair

Two-dimensional layered materials, such as graphene and MoS₂, are emerging as an exciting material system for a new generation of atomically thin electronic devices. With their ultrahigh surface to volume ratio and excellent electrical properties, 2D-layered materials hold the promise for the construction of a generation of chemical and biological sensors with unprecedented sensitivity. In my PhD thesis, I mainly focus on graphene based electronic biosensors and chemical sensors. In the first part of my thesis, I demonstrated the fabrication of graphene nanomesh (GNM), which is a graphene thin film with a periodic array of holes punctuated in it. The periodic holes introduce long periphery active edges that provide a high density of functional groups (e.g. carboxylic groups) to allow for covalent grafting of specific receptor molecules for chemical and

biosensor applications. After covalently functionalizing the GNM with glucose oxidase, I managed to make a novel electronic sensor which can detect glucose as well as pH change.

In the following part of my thesis I demonstrate the fabrication of graphene-hemin conjugate for nitric oxide detection. The non-covalent functionalization through π - π stacking interaction allows reliable immobilization of hemin molecules on graphene without damaging the graphene lattice to ensure the highly sensitive and specific detection of nitric oxide. The graphene-hemin nitric oxide sensor is capable of real-time monitoring of nitric oxide concentrations, which is of central importance for probing the diverse roles of nitric oxide in neurotransmission, cardiovascular systems, and immune responses. Our studies demonstrate that the graphene-hemin sensors can respond rapidly to nitric oxide in physiological environments with sub-nanomolar sensitivity. Furthermore, *in vitro* studies show that the graphene-hemin sensors can be used for the detection of nitric oxide released from macrophage cells and endothelial cells, demonstrating their practical functionality in complex biological systems.

In the last part of my thesis, I demonstrate the construction of few-layer molybdenum disulfide (MoS_2) based field-effect transistor (FET) device for highly sensitive detection of Hg^{2+} ion in aquatic solutions. The detection of mercury in aquatic environment is of great importance because mercury is an environment pollutant with severe toxicity. High binding affinity between mercury and sulfur makes MoS_2 a promising candidate for mercury sensing. Our studies demonstrate that MoS_2 sensors can selectively respond to Hg^{2+} ion with a detection limit of 30 pM. This MoS_2 FET based mercury sensor promises great potential for highly sensitive, label-free, low-cost, fast and non-aggressive detection of mercury in aquatic environment.

The dissertation of Shan Jiang is approved.

Richard B. Kaner

Qibing Pei

Xiangfeng Duan, Committee Chair

University of California, Los Angeles

2014

Table of Contents

ACKNOWLEDGEMENTS.....	vii
BIOGRAPHY.....	viii
INTRODUCTION.....	1
Chapter I: FABRICATION OF GRAPHENE NANOMESH AND ITS ELECTRONIC PROPERTIES	7
A. Fabrication of graphene nanomesh by block copolymer lithography	8
B. Results and discussion.....	9
Characterizations of graphene nanomesh structure	9
Electronic properties of graphene nanomesh	12
Chapter II: GRAPHENE NANOMESH BASED BIOSENSOR FOR GLUCOSE AND pH DETECTION	22
A. Experimental methods	23
Preparation of graphene nanomesh	23
Covalently functionalization of graphene nanomesh with glucose oxidase	23
Characterization of graphene nanomesh with glucose oxidase immobilized on top	24
B. Results and discussion.....	24
Detection of glucose	24
Detection of pH	26
Chapter III: REAL-TIME ELECTRICAL DETECTION OF NITRIC OXIDE IN BIOLOGICAL SYSTEMS WITH DUBNANOMOLAR SENSITIVITY	34
A. Experimental methods.....	37
Fabrication of graphene-hemin sensors	37

Characterization of graphene-hemin sensors	37
NO solution preparation	41
Electrical measurement	42
B. Results and discussion.....	42
Real-time electrical detection of NO	42
Selectivity and functionality in physiological solutions	46
Real-time monitoring of NO released by living cells	48
Chapter IV: HIGHLY SENSITIVE MERCURY(II) SENSOR BASED ON THIN-LAYERED MOLYBDENUM DISULFIDE FIELD-EFFECT TRANSISTOR	69
A. Experimental methods.....	70
Fabrication of MoS ₂ mercury sensor	70
Measurement of the electrical properties of the MoS ₂ device	71
B. Results and discussion.....	71
Sensitivity of the MoS ₂ Hg ²⁺ ion sensors	71
Investigation of the sensing mechanism	72
Selectivity of the MoS ₂ Hg ²⁺ ion sensors	72
CONCLUSION.....	77
REFERENCES.....	79

Acknowledgements

First of all, I owe my deepest gratitude to my doctoral committee Professor Richard B. Kaner, Professor Qibing Pei and Professor William M. Gelbart, who gave me valuable advices in my dissertation. I sincerely appreciate all their help. My advisor, Professor Xiangfeng Duan, spent lots of time and effort helping me not only about research but also about my professional skills. I am very grateful to him for sharing his opinions and giving me suggestions over many aspects of my graduate studying such as conducting experiments, completing research projects, doing presentations and writing papers. All of these have contributed to the accomplishment of my Ph.D. degree at UCLA. Many thanks also go to my group, including a collaborated group in Material Science and Engineering, advised by Professor Yu Huang, which have been very important for my graduate study. We shared experimental experiences, exchanged opinions on literatures and collaborated with each other. These help me quickly accumulate knowledge and experience in various fields, which absolutely complete me as a Doctor of Philosophy.

Additionally, I appreciate the collaboration with Professor Andre Nel, Dr. Xiang Wang and Professor Richard B. Kaner. Through discussion with them, I have obtained professional suggestions from their viewpoints which inspired my thinking and brought me more ideas for carrying out my research projects. I also would like to thank Dr. Adam Stieg for support in AFM facilities.

Finally, I would like to thank my family and friends. Without their support, guidance and help, I would never have been able to finish this dissertation.

Biography

Shan Jiang received her B.S. degree in Chemistry from Peking University, Beijing, China in 2009. She joined Dr. Xiangfeng Duan's group in 2009 and conducted the research of graphene based electronic biosensors and chemical sensors. She was awarded UCLA Summer Research Fellowship and Ralph & Charlene Bauer Research Award, Department of Chemistry and Biochemistry in 2009 and 2013, respectively. She has published ten research papers in peer-review scientific journals. She gave an oral presentation in Fall 2013 Materials Research Society Meeting in Boston. Her research interests include nanomaterials and electronic biosensors and chemical sensors.

INTRODUCTION

Graphene is two-dimensional crystalline form of carbon: a single layer of carbon atoms in a honeycomb lattice. This 2D structure is composed of triangular planar sub lattice of carbon-carbon σ bonds and a half-filled π band ¹. In 2004, Geim and co-workers successfully isolated atomic thin carbon layer by micro-mechanical cleavage method ². It is the unique optical property of graphene that lead to its discovery: this atomic thin material can be visualized with optical microscope due to its notable opacity when prepared on Si substrate with certain thickness of SiO₂ ³⁻⁵. Later on, it was discovered that graphene displayed distinctive Raman spectral characteristics, which was very powerful in distinguishing between single, double and multi-layer graphene (Figure 1-1b) ⁶⁻⁹. The simple technique of optical microscopy in conjunction with Raman spectroscopy greatly facilitated the scientific research on graphene based novel materials.

Graphene has arisen to be one of the most promising materials for fundamental studies and potential applications due to its fundamentally superior qualities ever since it was first experimentally discovered. The band structure of single layer graphene is determined to have 2D character and a linear dispersion relation of electronic wave functions with perfect electron-hole symmetry, in which Fermi surface consists of two cones touching at one singular, so-called Dirac point, where the density of states is zero (Figure 1-2a inset) ¹. The first demonstrated graphene device showed ambipolar field effect - the resistance showed a peak as a function of gate voltage where the charge carrier changed the sign at the conductance minimum, beside which the conductance increased linearly with gate voltage on both sides of the resistance peak (Figure. 1-2a) ^{10,11}. The in depth study of Shubnikov-de Haas oscillation revives the nature that charge carriers in single layer graphene is massless Dirac fermions- similar to relativistic

particles with zero rest mass with a Fermi velocity about 10^6 m/s¹². The observed charge carrier mobility can reach $200,000 \text{ cm}^2\text{V}^{-1}\text{s}^{-1}$ for both electrons and holes even at room temperature¹³. Unlike some other high mobility semiconductors, such as InSb which can only exhibit high mobility (mobility exceeding $60,000 \text{ cm}^2\text{V}^{-1}\text{s}^{-1}$ at room temperature) at a very low doping level with a 2D electron gas carrier concentration of 10^{11} cm^{-2} ¹⁴⁻¹⁵, graphene retains high mobility even with electron or hole doping with carrier density $> 10^{12} \text{ cm}^{-2}$ ^{13, 16-18}, enabling high current delivery through the device. The observation of quantum hall effect at room temperature also indicated exceptional electronic quality of graphene crystals^{12, 19-21}. These extraordinary electrical properties make graphene a good candidate for high frequency device applications. Wafer scale gigahertz graphene transistors with cut-off frequency as high as 100GHz was demonstrated²². This recorded was recently increase to 150 GHz in CVD grown graphene by IBM research group and to 300 GHz in mechanical exfoliated graphene by UCLA researchers²³⁻²⁴.

Like other semiconductor materials, the electrical properties of graphene change as the device dimension shrinks to nanometer regime in which quantum confinement and edge effect are taken into account^{1, 25-27}. Various graphene based nanostructures, such as graphene nanoribbons (GNRs), graphene nanomesh, graphene quantum dots have been fabricated. Interesting semiconducting band gaps were predicted in (GNRs) with width under 100nm. The existence of tunable band gap and localized edge state in graphene nanostructures intrigues a lot of research interest and experimental efforts to fabricate them and study their transport properties.

Due to its unique electronic properties, graphene is promising for a wide range of applications. Chemical sensors and biosensors have been one of these applications.

Graphene is of increasing interest for the development of highly sensitive label-free chemical and biological sensors due to its unique combination of several important characteristics. The exceptionally high carrier mobility and the single-atom thickness with the largest possible surface to volume ratio can lead to ultra-high sensitivity in graphene-based sensors. Graphene has inherently low electrical noise due to the quality of its crystal lattice and its two-dimensional nature which can screen the charge fluctuations. Graphene also has practical advantages for making sensors such as its high chemical stability and the amenability to making devices by conventional lithographic approaches.²⁸ The graphene nanoelectronic devices based chemical and biological sensors have other advantages such as decreased energy consumption and miniaturized size.²⁹

Graphene based biosensors can detect various biological species under physiological conditions. Research of graphene sensors working in solution started with pH sensing tests, with a solution-gated GFET.³⁰ A narrow p-n plateau region near the Dirac point was observed, while capacitive charging of the graphene/solution interface can induce both electron and hole conduction. As pH increases, OH⁻ adsorption p-dopes the channel, shifting the Dirac point towards positive potential. Charge transport in solution can be significantly affected by aqueous ions that screen impurity charges in the device.^{31,32} A solution-gated GFET showed high transconductance and electronic detection of pH and protein adsorption with a linear dependence of conductance with electrolyte pH.³³ Additionally, the conductance increased with exposure to picomolar concentrations of a protein through non-specific absorption. Suspended graphene was found to exhibit higher transconductance in the linear operating modes and less low-frequency noise than GFETs supported on SiO₂ substrates.³⁴ The rGO based sensor

devices have also demonstrated real-time, label-free detection of the hormonal catecholamine molecules secreted from living cells.³⁵

Although bare graphene devices showed high sensitivity toward biomolecules, there is usually a lack of specificity, which is necessary for any practical sensors. To this end, it is useful to functionalize graphene with receptors that selectively bind to specific target species. With the attachment of specific receptors, CMG biosensors are used to detect bacterium and DNA.³⁶ Aptamer modified GFET showed high sensitivity and good selectivity toward Immunoglobulin E (IgE) protein. The dissociation constant of IgE and the aptamer was calculated according to the calibration curve. By noncovalently immobilizing single-stranded DNA probes on CVD graphene devices, a DNA sensor can be created for the detection of specific target DNA with the capability to distinguish the mismatch of single-base pairs with a detection limit of 0.01 nM.³⁶ The sensing mechanism was attributed to n-doping based on interactions of the nucleotides with the graphene channel.

In my PhD thesis, I mainly focus on graphene based electronic biosensors and chemical sensors. I have used different methods to functionalize graphene to make it specifically respond to different compounds or species. One of these methods is the fabrication of graphene nanomesh (GNM), which is a graphene thin film with a periodic pattern of holes punctuated in it. The periodic holes introduce lateral charge confinement to induce a sufficient transport gap for room temperature transistor operation. Furthermore, the long periphery active edges provide a high density of functional groups (e.g. carboxylic groups) to allow for covalent grafting of specific receptor molecules for chemical and biosensor applications. After covalently functionalizing the GNM with

glucose oxidase, I managed to make a novel electronic sensor which can detect glucose as well as pH change. The other method I used to functionalize graphene is the fabrication of graphene-hemin conjugate. The non-covalent functionalization through π - π stacking interaction allows reliable immobilization of hemin molecules on graphene without damaging the graphene lattice to ensure the highly sensitive and specific detection of nitric oxide. The graphene-hemin nitric oxide sensor is capable of real-time monitoring of nitric oxide concentrations, which is of central importance for probing the diverse roles of nitric oxide in neurotransmission, cardiovascular systems, and immune responses. Our studies demonstrate that the graphene-hemin sensors can respond rapidly to nitric oxide in physiological environments with a sub-nanomolar sensitivity. Furthermore, *in vitro* studies show that the graphene-hemin sensors can be used for the detection of nitric oxide released from macrophage cells and endothelial cells, demonstrating their practical functionality in complex biological systems. Beside graphene, other two-dimensional layered materials, such as MoS₂ and WSe₂, are also emerging as an exciting material system for a new generation of atomically thin electronic devices. With its ultrahigh surface to volume ratio and excellent electrical properties, few-layer MoS₂ holds the promise for unprecedented sensitivity for sensing application. High binding affinity between mercury and sulfur makes MoS₂ a promising candidate for mercury sensing, which is of great importance because mercury is an environment pollutant with severe toxicity. In the last part of my thesis, I constructed a few-layer molybdenum disulfide (MoS₂) based field-effect transistor (FET) device for highly sensitive detection of Hg²⁺ ion in aquatic solutions. Our studies demonstrate that MoS₂ sensors selectively respond to Hg²⁺ ion with a detection limit of 30 pM. This MoS₂

FET based mercury sensor promises great potential for highly sensitive, label-free, low-cost, fast and non-aggressive detection of mercury in aquatic environment.

Chapter I: FABRICATION OF GRAPHENE NANOMESH AND ITS ELECTRONIC PROPERTIES

Graphene is particularly attractive for the application of chemical sensors and biosensors due to its unique combination of several important characteristics.^{1,2} The exceptionally high carrier mobility¹⁰ and the single-atom thickness with the largest possible surface to volume ratio can lead to ultra-high sensitivity in graphene-based sensors.^{28,29} However, the pristine graphene is generally chemically inert, and difficult to be functionalized with specific chemical receptors for sensing applications. Additionally, graphene is a semimetal with zero band gap and cannot be used for effective field-effect transistors (FETs) at room temperature.

In this Chapter, we report the production of a new graphene nanostructure - which we call graphene nanomesh. Graphene nanomesh is a single or few-layer of graphene with a high density periodic array of nanoholes punched in.³ The periodic holes introduce lateral charge confinement to induce a sufficient transport gap for room temperature transistor operation. Furthermore, the long periphery active edges provide a high density of functional groups (e.g. carboxylic groups) to allow for covalent grafting of specific receptor molecules for chemical and biosensor applications. The nanomeshes are prepared with block copolymer lithography and can have variable periodicities and neck widths down to 5 nm. Graphene nanomesh field-effect transistors can support currents nearly 100 times greater than individual graphene nanoribbon devices, and the on-off ratio - which is comparable with the values achieved in individual nanoribbon devices - can be tuned by varying the neck width. The block copolymer lithography approach used to make the nanomesh devices is intrinsically scalable and could allow for the rational

design and fabrication of graphene-based devices and circuits with standard semiconductor processing.

A. Fabrication of graphene nanomesh by block copolymer lithography

Graphene thin film was obtained by mechanically peeling of natural graphite on to silicon substrate with 300 nm thermal oxide. A 10 nm SiO_x thin film was evaporated onto graphene using e-beam evaporator operated at 10⁻⁶ torr. This fresh oxide surface was functionalized with P(S-r-MMA) random copolymer (Polymer Source, Mn: 11000, Mw/Mn: 1.15, styrene 55 mol%, functionalized α -hydroxyl and ω -tempo moiety) by spin coating a thin film from 1 wt% toluene solution. This film was annealed at 170 °C for 72 hours to anchor the polymer onto oxide surface through end hydroxyl group, and then rinsed with toluene to remove unanchored polymer. P(S-b-MMA) with molecular weight of 77000 g mol⁻¹ (PS-PMMA: 55000-22000, Mw/Mn: 1.09) and 47700 g mol⁻¹ (PS-PMMA: 35500-12200, Mw/Mn: 1.04) were purchased from Polymer Source and dissolved in toluene. The block copolymer thin film was prepared on the neutralized surface by spin coating 1 wt% filtered polymer solution at 2500 rpm followed by annealing at 180 °C for 12 hours. The thickness was determined to be 30-35 nm by AFM profile. Annealed film was exposed to 295 nm UV irradiation for 30 min under vacuum. The degraded PMMA domains were removed by immersing in glacial acid for 20 min followed by extensive water rinsing.

We used reactive ion etcher (STS MESC Multiplex Advanced Oxide Etcher) to etch down to graphene layer. Firstly, an O₂ plasma process (50 W, 4 mTorr) was used to remove exposed random copolymer. Controlled over etching here can be used to enlarge the nanoholes in PS nanomesh. Then, CHF₃ plasma (50 W, 6 mTorr) was employed to

punch holes into evaporated SiO_x to expose underlying graphene layer. Additional O₂ plasma was used to completely etch away exposed region of graphene or to further undercut the graphene nanomesh.

B. Results and discussion

Characterizations of graphene nanomesh structure

TEM samples were prepared by spin coating 300 nm thick of PMMA polymer resist onto the graphene mesh substrate and baked at 100 °C. The PMMA-graphene mesh film was then lifted off in HF solution and transferred onto the lacey film coated copper grid. After PMMA was removed by acetone vapour, the sample was characterized by JEOL 1200 operated at 80kV. Tapping mode AFM was done with a Veeco 5000. SEM imaging was performed on a JEOL 6700F operated at 5 kV.

The Graphene nanomesh (GNM) reported here is a single or few-layer of graphene with a high density array of nanoscale holes punched in (Figure 1-1g). For the convenience of discussion, we define two critical structural parameters in a GNM: the "periodicity" defined as the center-to-center distance between two neighboring nanoholes, and the "neck width" defined as the smallest edge-to-edge distance between two neighboring nanoholes in the nanomesh.

Figure 1-1 illustrates our approach to fabricate GNMs. For initial demonstrations, we use mechanically peeled graphene flakes as the starting material, although the approach described here can be readily extended to graphene films obtained through chemical exfoliation or chemical vapour deposition³⁷⁻³⁹. A 10 nm thick silicon oxide (SiO_x) film is first evaporated onto graphene as the protecting layer and also the grafting

substrate for the following block copolymer nanopatterning⁴⁰. The poly(styrene-block-methyl methacrylate) (P(S-b-MMA)) block copolymer thin film with cylindrical domains normal to the surface is then fabricated and used as the etching template⁴⁰, and a CHF₃ based reactive ion etch (RIE) process followed by oxygen plasma etch is employed to punch holes into the graphene layer.

Atomic force microscopy (AFM) image of the annealed P(S-b-MMA) thin film shows the cylindrical PMMA domains packed hexagonally within the PS matrix (Figure 1-2a). The domain center-to-center distance is approximately 39 nm by using P(S-b-MMA) with a molecular weight of 77,000 g mol⁻¹ and a PS:PMMA volume ratio of 70:30. Changing the molecular weight while keeping the volume ratio constant can result in vertical aligned domains with variable center-to-center distance⁴¹. After UV exposure and glacial acid development to remove PMMA domains, a porous structure of PS matrix with hexagonally arranged nanoholes vertically penetrating through the film is obtained (Figure 1-2b). The following etching process drills into the underneath SiO_x layer, leaving a SiO_x nanomesh that can serve as the mask for subsequent oxygen plasma etch to form GNMs (Figure 1-2c). The oxide mask can be easily removed by briefly dipping the sample into HF solution and the GNM structure can be seen under SEM (Figure 1-2d).

To unambiguously determine the GNM structure, we have carried out extensive transmission electron microscopy (TEM) studies (see Methods for details). Figure 1-3a-h shows a series of TEM images of the GNMs with variable periodicities or neck widths. For better image contrast, most TEM images are taken from GNMs with a relative large thickness (5-10 nm), although images of GNMs with one or a-few-layer graphene have

also been obtained but typically with lower contrast. TEM studies clearly shows GNM structure with nearly hexagonally arranged nanoholes, consistent with SEM studies. Figures 1-3a and e show TEM images of a GNM obtained from copolymer mask with molecular weight of 77000 g mol^{-1} , with a nanohole periodicity of ca. 39 nm, and average neck width of 14.6 nm. The nanoholes observed here are slightly larger than the PMMA domains in the self-assembled block copolymer pattern due to slight over etch in the fabrication process. Importantly, such nanomesh structure can be readily seen over many microns and apparently is only limited by the size of starting graphene flakes (Figure 1-4).

Our fabrication process shows great versatility in controlling both the neck width and the periodicity independently. For example, the neck width can be tuned through controlled over etching during the fabrication process. Figures 1-3b and f show the TEM images of a nanomesh with the same periodicity of ca. 39 nm, but smaller average neck width of 11.2 nm through controlled lateral over etch of PS mask. Figures 1-3c and g show a nanomesh with average neck width of 7.1 nm obtained with additional over etch. Furthermore, it is also possible to tune the mesh periodicity and neck width by using block copolymer of different molecular weight⁴¹. Figures 1-3d and h show a much denser GNM with smaller periodicity of ca. 27 nm and average neck width of 9.3 nm obtained using smaller molecular weight block copolymer thin film as the mask template.

As the GNM neck width represents the smallest dimension that controls charge transport through the system, we have carried out statistical analysis of the neck widths of the GNMs obtained with variable etching conditions or different block copolymer masks (Figure 1-3i-l). The histograms resulted from the statistic analysis show that a series of GNMs with variable neck widths of 14.6, 11.2, 7.1 and 9.3 nm have been achieved. The

standard deviation of the GNM neck width is in general less than 2 nm. The smallest neck width we observed to date is about 5 nm through even more aggressive over etching (Figure 1-5). In this deep nanometer regime, this aggressive over-etch may lead to the breakage of some necks in the nanomesh due to a finite standard deviation, and the yield can be limited. However, we note our block copolymer assembly process is not yet optimized to the best it can offer, and the optimization of the block copolymer self-assembly can lead to more uniform nanomesh that afford more aggressive over etch for even smaller neck width^{42,43}. These TEM studies clearly demonstrate that highly uniform GNMs can be obtained with controllable periodicities and neck widths using the block copolymer nanolithography.

Electronic properties of graphene nanomesh

This ability to control the nanomesh periodicity and neck width is very important for controlling their electronic properties because charge transport properties is highly dependent on the width of critical current pathway. In the case of graphene nanoribbons (GNRs), both theoretical and experimental works have shown that the size of the conduction band gap is inversely proportional to the ribbon width. The GNMs can be viewed as a highly interconnected network of GNRs. Therefore, narrow neck width is needed to gain enough bandgap for sufficient gate response and on-off ratio, and denser mesh structure can enable higher current delivery.

To investigate the electronic properties of the GNMs, we have fabricated GNM based transistors and carried out electrical transport studies. A three terminal device is fabricated using the GNM as the semiconducting channel, e-beam evaporated Ti/Au pads as the source-drain contacts, a highly doped p-type silicon substrate as the back gate and

a 300-nm thermal oxide as the gate dielectric (Figure 1-6a, b). Figures 1-6 c and d show the electrical transport characteristics of a typical GNM transistor with estimated neck width of ca. 10 nm. Drain current (I_d) versus drain-source voltage (V_d) relations at various gate voltages (V_g) for the GNM transistor show typical p-channel transistor behaviour (Figure 1-6c). The hole-doping observed in the GNM is similar to GNR devices, and can be attributed to edge oxidation in the O_2 plasma process or physisorbed oxygen from the ambient and other species during the sample preparation steps. The plots of I_d versus V_g (Figure 1-6d) at a constant $V_d = -10$ mV, -100 mV and -500 mV show little current when the V_g is more positive than a threshold voltage (V_{th}) of -0.6 V, and I_d increases nearly linearly when the V_g increases in the negative direction. The plot shows the device has an on-state conductance as high as $550 \mu\text{S}$ at $V_g = -10$ V, which is comparable to an array of ~ 50 - 100 parallel GNR devices⁴⁴. The I_d - V_g plots also show the device has an on-off ratio greater than 10, which is comparable to GNR FETs with width in the range of 10 - 15 nm⁴⁴. Importantly, the on-off ratio of the GNM devices can be readily tuned by varying neck width. Additional electrical studies show smaller on-off ratio of 6 for GNM device with larger neck width (~ 15 nm), and higher on-off ratio of more than 100 for GNM device with smaller neck width (~ 7 nm) (Figure 1-7). This observation is consistent with GNR devices where the conduction band gap and on-off ratio is inversely proportional to the width or the critical current pathway. Similar to GNRs, the opening of the conduction band gap in our GNM structure can be attributed to a combination of multiple factors including lateral quantum confinement and localization effect resulted from edge disorder such as variable edge roughness or absorbed species in oxygen plasma etching process^{45,46}. Elucidation of the exact origin of the band gap and

investigation of the impact of exact edge termination will be an interesting topic in future studies. We believe the on-off ratio can be further increased upon additional shrinking the GNM neck width. These studies clearly demonstrate the formation of GNMs can effectively enable a semiconductor thin film with neck-width tunable electronic properties.

In summary, we have demonstrated a new graphene nanostructure — graphene nanomesh — that can effectively open up a conduction band gap in a large piece of graphene to form a continuous semiconducting thin film. We have shown that GNMs with variable periodicities and neck widths down to 5 nm can be prepared using block copolymer lithography. Using such nanomesh as semiconducting channel, we have demonstrated room temperature transistors with driving current nearly 100 times larger than those of individual GNR device, whilst with a comparable on-off ratio that is tunable by varying the neck widths. Further optimization of the process can lead to GNMs with smaller periodicities and smaller neck widths to allow even higher on-off ratio and larger driving current. The block copolymer lithography fabrication of GNMs is an intrinsically scalable approach, and can therefore enable a continuous semiconducting GNM thin film that can be processed using standard semiconductor processing to fabricate integrated devices/circuits with designed characteristics to meet specific circuit requirements. The availability of such GNMs in deep nanometer regime will also provide an interesting system for fundamental investigation of transport behaviour in the highly interconnected graphene network and open exciting opportunities in highly sensitive biosensors and a new generation of spintronics.

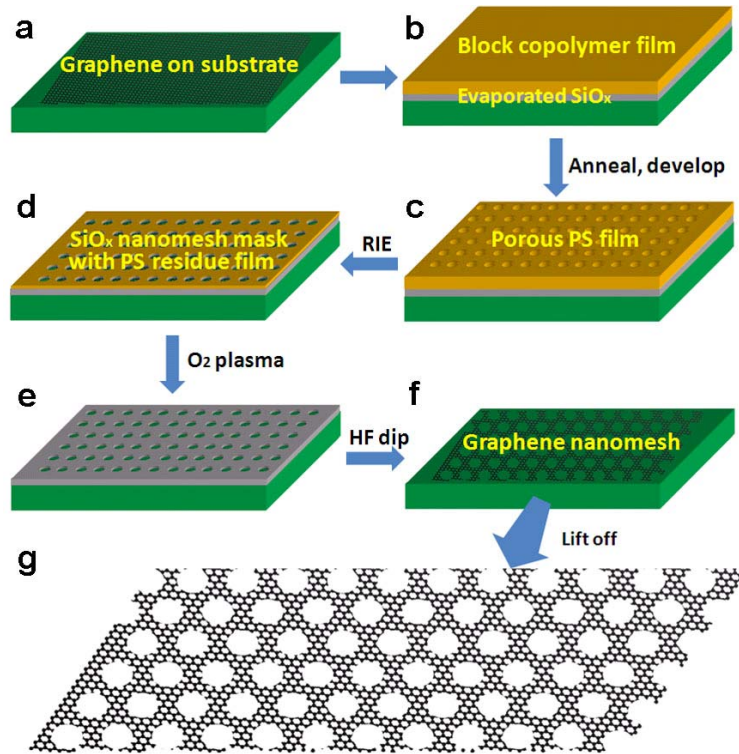


Figure 1-1 Schematic of making graphene nanomesh. (a) A pristine graphene flake on top of silicon oxide substrate as starting material. (b) The graphene flake is covered by a thin layer of evaporated SiO_x and a thin film of spin coated block copolymer poly(styrene-block-methyl methacrylate) (P(S-b-MMA)). The SiO_x here is used as protecting layer and the grafting substrate for the following block copolymer nanopatterning. (c) The P(S-b-MMA) block copolymer film is annealed and developed, leaving the porous PS matrix as nanomesh template for further patterning. (d) Fluoride based reactive ion etching (RIE) to penetrate oxide layer and partially degrade PS film, and form SiO_x nanomesh hard mask. (e) Graphene in the exposed area is etched away by O₂ plasma. (f) After HF dip to remove oxide mask, a GNM is obtained. (g) Free standing GNM can be lifted off from the substrate by etching away underlying silicon oxide.

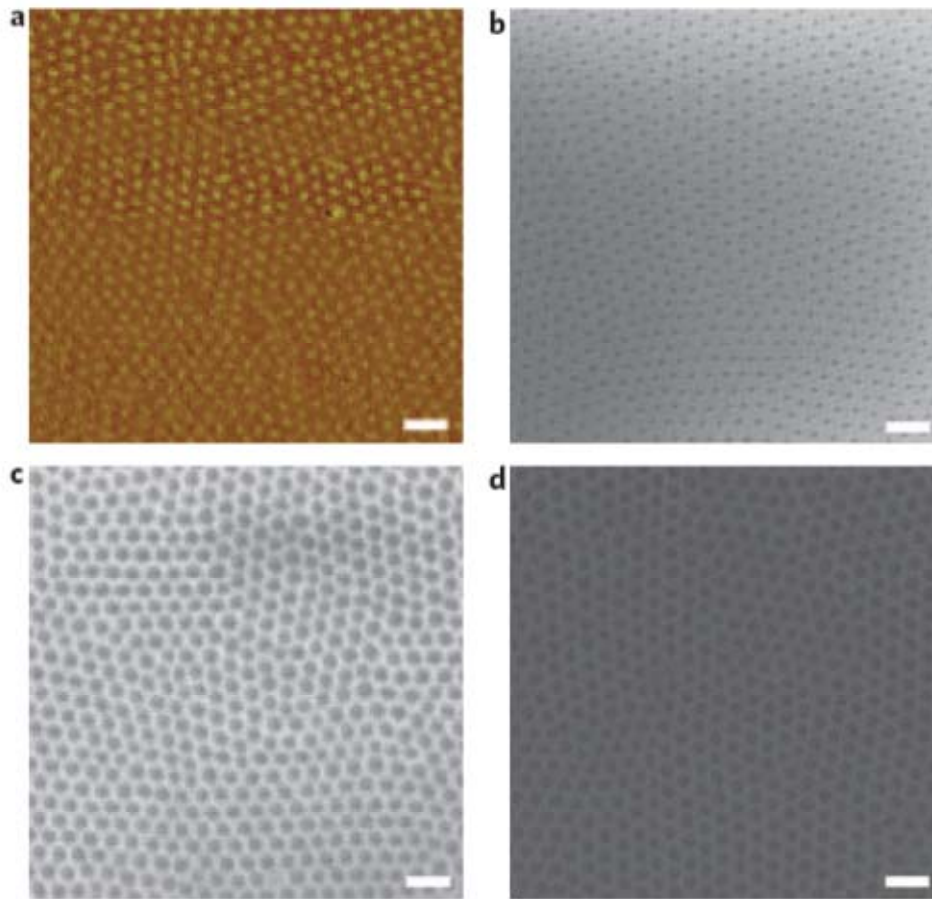


Figure 1-2 Images illustrating steps of nanomesh fabrication process. (a) An AFM phase contrast image of the annealed block copolymer film on graphene shows hexagonal packed PMMA domains in the PS matrix. (b) An SEM image of a porous PS film obtained by selectively removing the PMMA domains. (c) An SEM image of the SiO_x nanomesh mask after reactive ion etching with PS mask. (d) An SEM image of a GNM structure after removing top SiO_x mesh mask. All scale bars indicate 100 nm.

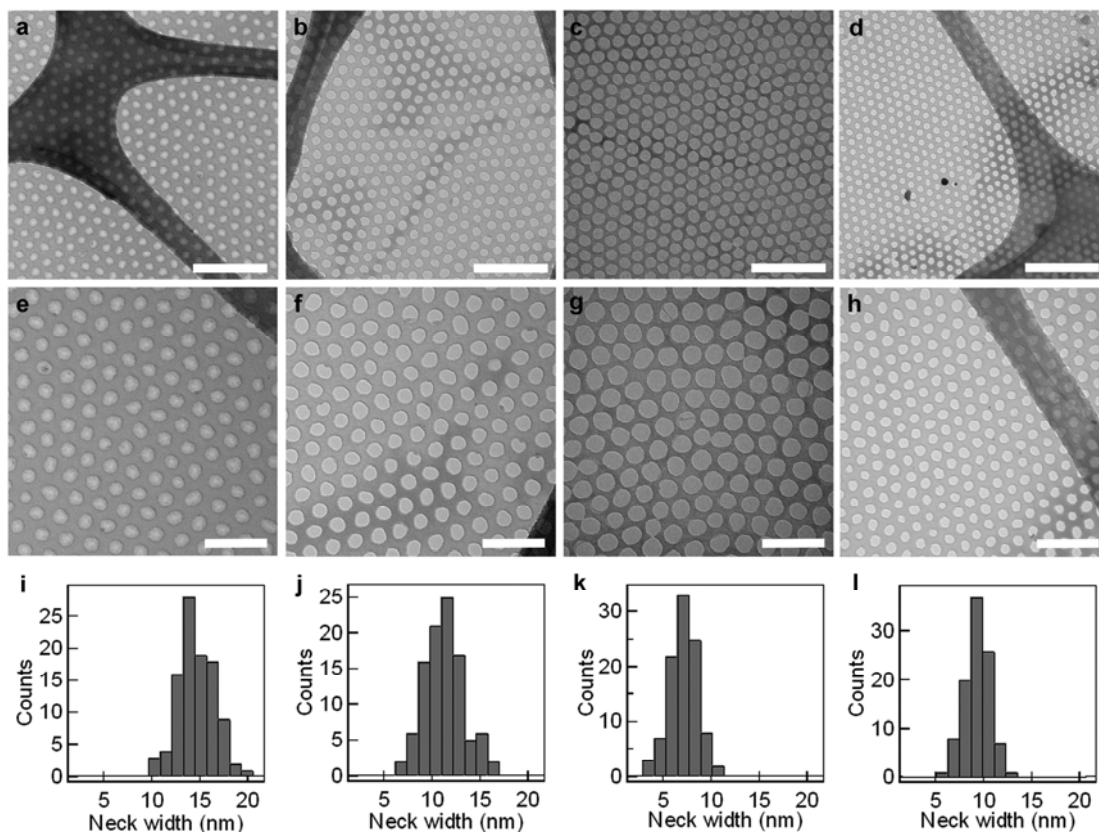


Figure 1-3 TEM studies of graphene and thin layer graphite nanomesh. (a) (e) TEM images of GNMs with periodicity of 39 nm and neck width of 14.6 nm obtained with block copolymer P(S-b-MMA) of molecular weight of 77000 g mol^{-1} . (b) (f) GNM with periodicity of 39 nm and neck width of 11.2 nm obtained with controlled over etching. (c) (g) GNM with periodicity of 39 nm and neck width of 7.1 nm obtained with additional over etching. (d) (h) GNM with periodicity of 27 nm and neck width of 9.3 nm obtained with block copolymer P(S-b-MMA) of smaller molecular weight of 47700 g mol^{-1} . The dark strips in the background of the images originate from the lacy carbon on TEM grids. Scale bars for (a-d) indicate 200 nm and scale bars for (e-h) indicate 100 nm. i-l, Histograms of the GNM neck width for (e-h) with average neck widths of 14.6 nm,

11.2 nm, 7.1 nm and 9.3 nm; and standard deviations of 2.0 nm, 1.9 nm, 1.5 nm and 1.3 nm, respectively.

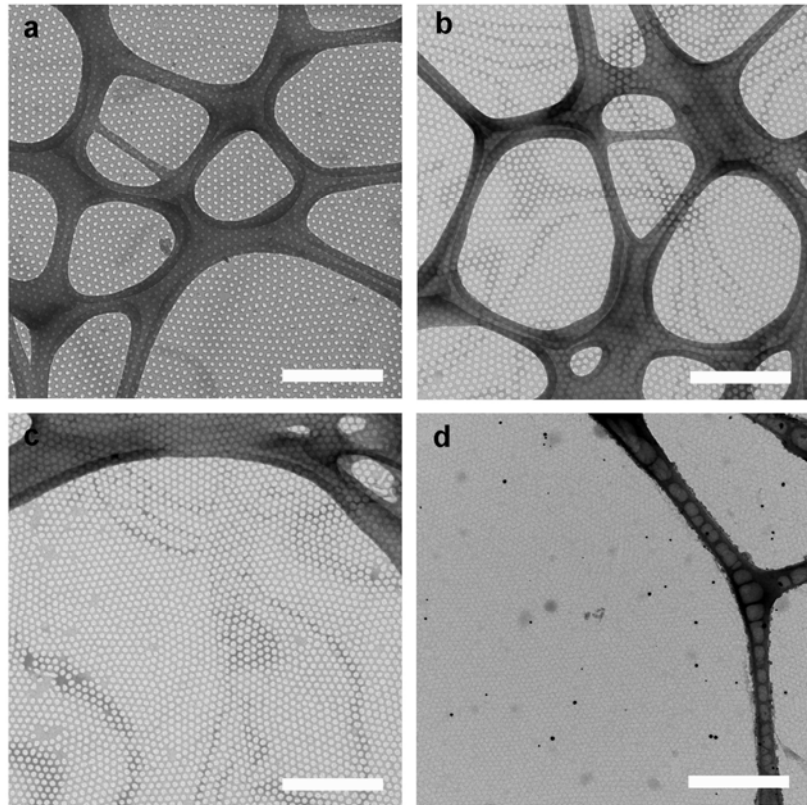


Figure 1-4 Low magnification TEM image of GNMs with periodicity of 39 nm and neck width of (a) 14.6 nm, (b) 11.2 nm, (c) 7.1 nm, and (d) periodicity of 27nm and neck width 7.8 nm. All scale bars indicate 500 nm. The nanomesh structure can extend up to several microns. The only limitation is the size of graphene flakes, indicating the possibility to fabricate such nanomesh structure on wafer scale, in conjunction with the recent advances in growth of graphene over large area substrate.

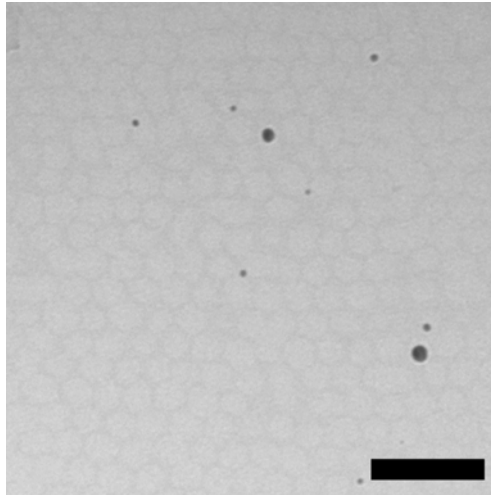


Figure 1-5 TEM image of graphene nanomesh with neck width of ~ 5 nm. Scale bar indicates 100 nm.

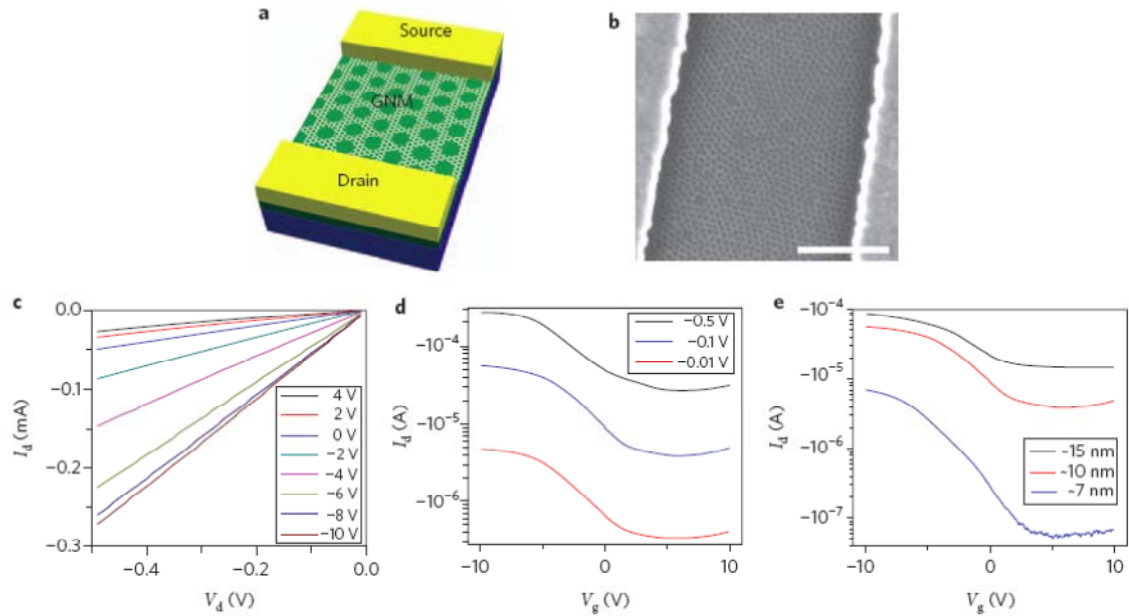


Figure 1-6 Room temperature electrical properties of graphene nanomesh device. (a) A schematic of a GNM-FET. The device is fabricated on heavily doped silicon substrate with 300-nm SiO₂ as the gate dielectric. The electronic measurement was done in ambient at room temperature without removing top oxide layer. (b) An SEM image of a GNM device made from nanomesh with a periodicity ca. 39 nm, and neck width of ca. 10 nm. Scale bar indicates 500 nm. (c) Drain current (I_d) versus drain-source voltage (V_d) recorded at different gate voltage for a GNM device with channel width of $\sim 2 \mu\text{m}$ and channel length of $\sim 1 \mu\text{m}$. The on state conductance at $V_g = -10 \text{ V}$ is comparable to an array of 100 parallel GNR devices. d, Transfer characteristics for the device in (c) at $V_d = -10 \text{ mV}$, -100 mV and -500 mV . The ratio between I_{on} to I_{off} for this device is ~ 14 at $V_d = -100 \text{ mV}$. e, Transfer characteristics at $V_d = -100 \text{ mV}$ for GNMs with different estimated neck widths of $\sim 15 \text{ nm}$ (device channel width $6.5 \mu\text{m}$ and length $3.6 \mu\text{m}$), $\sim 10 \text{ nm}$ (channel width $2 \mu\text{m}$ and length $1 \mu\text{m}$), and $\sim 7 \text{ nm}$ (channel width $3 \mu\text{m}$ and length $2.3 \mu\text{m}$).

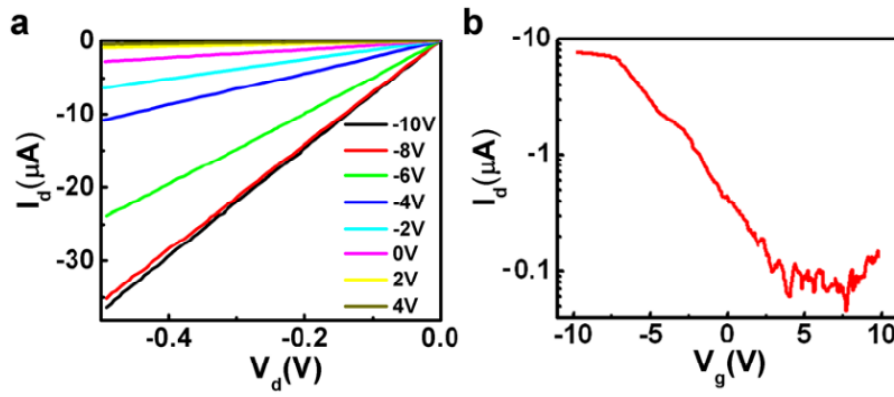


Figure 1-7 Device characteristics for a high on-off (~ 100) GNM device. (a) Output I_d - V_d relation at variable gate voltages for the device. The device has a channel width $3.5 \mu\text{m}$ and channel length $2 \mu\text{m}$. (b) Transfer characteristics I_d - V_g at $V_d = -100$ mV.

Chapter II: GRAPHENE NANOMESH BASED BIOSENSOR FOR GLUCOSE AND pH DETECTION

Glucose sensor is of great research interest⁴⁷⁻⁵⁰ because of the importance of monitoring and control of blood glucose concentration in diabetes care. Up to now, most glucose sensors are based on electrochemical reactions by using amperometric enzyme electrodes⁵¹⁻⁵³. Among those, a lot of work concentrated on third generation of glucose sensors which work without redox mediator and independent of oxygen, because of their potential for in vivo blood glucose sensing. Less attention was paid to conductivity based glucose sensors probably because uncharged glucose molecule does not change the conductivity of device through the traditional affinity based electrostatic sensing mode⁵⁴⁻⁵⁸.

In this chapter, we demonstrate the use of graphene nanomesh (GNM) as biosensor for glucose and pH detection. For glucose detection, glucose oxidase (GOx) is covalently attached onto GNM. Adding glucose leads to the positive shift of Dirac point of GOx functioned GNM, which is attributed to doping effect of hydrogen peroxide generated by GOx catalyzed reaction. Real time stepwise response is observed with addition of glucose, indicating the capability of GOx functioned GNM to be a glucose sensor. GNM device also acts as a pH sensor with apparently rising of conductance upon increase of pH.

Here we report the capability of GNM device as an effective glucose sensor and pH sensor. High density of carboxylic group on the GNM edge makes it an effective pH sensor because the sensing does not rely on physically absorption of H⁺ or OH⁻ on to

GNM⁵⁹. Instead, the pH change of the solution alters the degree of dissociation of carboxylic groups on the GNM edges, and thus changes the conductance through electrostatic gating effect. As for glucose sensing, we proposed a new sensing mechanism based on doping effect of H₂O₂ to GNM. This proposed a possibility to make solid state transistor based glucose sensor with high sensitivity and fast response speed. Moreover, the nanoscale GNM glucose sensor consumes little oxygen due to the small size. It does not rely on oxygen concentration, and does not need redox mediator, either. This provides the potential for in vivo detection of blood glucose⁵⁶.

A. Experimental methods

Preparation of graphene nanomesh

Graphene was prepared by mechanical exfoliation onto Si substrate with 300nm thermal oxide layer. The GNM was obtained by diblock copolymer nanolithography and oxygen plasma treatment, and the FET device was fabricated through e-beam lithography and metallization process.

Covalently functionalization of graphene nanomesh with glucose oxidase

For glucose sensor application, GOx was covalently immobilized onto the GNM through carbodiimide coupling reaction between carboxylic groups on GNM and amino groups on GOx⁶⁰⁻⁶². Carboxylic groups were introduced by treatment of oxygen plasma during the fabrication of GNM. The chemical structure of GOx immobilized GNM is illustrated in Figure 2-1 (a). Briefly, the GNM device was first immersed in 98% H₂SO₄ for 30 minutes to further oxidize the GNM edge in order to increase the density of carboxylic groups. After thoroughly washed with DI water, the sample was treated with

freshly prepared EDC (100mmol/L) and NHS (250mmol/L) to form the reactive ester. Then the sample was washed with DI water and immediately transferred into a 10mg/mL GOx solution in pH 7.0 PBS. The enzyme immobilization process was kept for 12 hours at room temperature. This allowed GOx to covalently link to the edge of GNM through amide linkage. At the end, the sample was washed thoroughly with DI water to remove non-covalent bonded GOx from GNM.

Characterization of graphene nanomesh with glucose oxidase immobilized on top

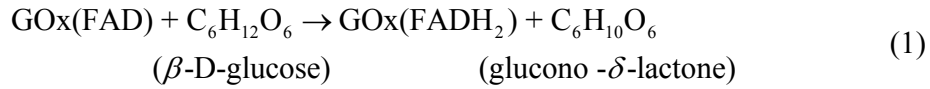
We use Atomic Force Microscopy (AFM) to characterize the GNM sample before and after the GOx immobilization. As shown in Figure 2-2 (a) and (c), the height of GNM before GOx immobilization is about 12 nm. This height includes the thickness of GNM and the etching depth of the nanoholes into the SiO₂. As shown in Figure 2-2 (b) and (d), after GOx immobilization the height is about 15-20 nm. The increased height is consistent with diameter of GOx, indicating that GOx is successfully immobilized onto GNM.

B. Results and discussion

Detection of glucose

The sensing measurement is carried out in aqueous solution, with pre-deposited Ti/Au pad as solution gate electrode. In this case, the electrochemical double layer acts as an effective top gate insulator⁶³. Glucose solution of different concentration was dropped directly on top of the GNM device with a PDMS well placed on top of the substrate to confine the liquid, as illustrated in Figure 2-1 (b). All sensing experiments are carried out at room temperature. Figure 2-3 (a) shows the conductance plotted against solution gate

voltage V_g in aqueous solution for bare GNM device without GOx function. We observed the ambipolar field effect characteristic of the GNM device. After introducing 0.9 mM glucose solution, we observed a slightly shift of Dirac point to negative direction, However, the electrical characteristics did not change further with higher glucose concentration. This negative shift of dirac point might be attribute to the absorption and doping effect of glucose onto GNM. On the other hand, the Dirac point of GOx immobilized GNM device kept shifting to positive direction with increasing glucose concentration, as showed in Figure 2-3(b). The differences between bare GNM device and GOx immobilized GNM device suggest that immobilization of GOx is responsible for the positive dirac point shift.



As shown above, the GOx catalyze two step reactions upon adding glucose solutions. First, β -D-glucose transfers two electrons to flavin adenine dinucleotide (FAD) – the active center of GOx. FAD is reduced to FADH₂, and β -D-glucose is oxidized to glucono δ -lactone. Then, FADH₂ is oxidized by oxygen to FAD, and oxygen is reduced to hydrogen peroxide (H₂O₂). In previous report, the electron transfer could occur from the top of the valence band of graphene to the lowest unoccupied molecular orbital (LUMO) of H₂O₂^{50,64}. In our system, H₂O₂ generated by oxygen reduction diffuses and absorbs onto the surface of GNM. The electron transfer from top of the valence band of

graphene to the LUMO of H_2O_2 will increase the hole concentration in GNM device, decrease the Fermi level and thus increase the Dirac point voltage, similar to electrical static p-type doping effect.

To prove this mechanism, we introduced H_2O_2 solution to a GOx immobilized GNM device. The solution of H_2O_2 was prepared as the same concentration as the glucose solution, since one mole glucose will generate equal mole H_2O_2 in the redox reaction. Figure 2-4 shows the conductance versus solution gate voltage curve of the GOx immobilized GNM device in different H_2O_2 concentrations. As expected, the Dirac point shifted to positive direction as H_2O_2 concentration increasing, indicated that the generation of H_2O_2 through the GOx catalyzed reaction may be the reason of the positive shift of the Dirac point of GNM glucose sensor.

To prove the selectivity of our GNM sensor, we added fructose and galactose water solution and no obvious conductance change was found (Figure 2-5). However, with addition of glucose solution, the conductance increased apparently at -0.4 V solution gate bias, which is consistent with Dirac point shifting to positive direction. We also found that after the addition of glucose solution, the conductance increased first but then decreased after tens of seconds. This may be attributed to the decreasing of local pH by formation of gluconic acid through hydrolysis of glucono- δ -lactone - the oxidation product of β -D-glucose. According to the conductance versus gate voltage measurement, hole is the carrier at this condition. The conductance of GNM device will decrease with decreasing pH by reducing the negative static charge gating effect.

Detection of pH

We also use the GNM device for pH sensing test without further treatment. Different pH solution was made by mixing phosphate buffer solution (PBS), hydrochloric acid solution and sodium hydroxide solution. No back gate or solution gate potential was applied during the measurement. Figure 2-6 plots the conductance of the GNM device against the change of the solution. The conductance increased stepwise with increasing the pH. The GNM is p-doped due to edge oxidation and absorption of oxygen species during the fabrication process. With increasing pH, the carboxylic groups at nanoholes edges dissociate to a higher degree, leaving more negative charge around the GNM channel. This negative gate effect increases the hole concentration and thus the conductance of the GNM device.

We also need to argue that the conductance increase of GOx immobilized GNM device as introduction of glucose solution does not come from the redox current. Figure 2-1 (c) is the circuit diagram of our electrical measurement system⁶⁵. In our system, source and drain electrodes are bridged with GOx immobilized GNM. So they together can be considered as working electrode. And the solution gate electrode is considered as the counter electrode. At -0.4V solution gate, the working electrode is at higher potential than the counter electrode, so the current will go from working electrode to counter electrode through the solution, which means electrons transfer from glucose to FAD center of GOx and then directly transfer to GNM and the electrode. If the mechanism is amperometric, the drain current would go down as glucose solution is introduced, which is opposite from our observations. Also, we measured the leakage current at $V_{ds}=0$ whereas V_g swept from -0.8V to 0.8V. The leakage current is about -5 nA at $V_g=-0.4V$ where we did real time measurement, which is negligible compare to our device current.

Our GNM sensor has intrinsic advantage over graphene sensor due to its large number of chemical active sites. As a comparison, we make graphene glucose sensor through the same fabrication process. Figure 2-7 (a) shows conductance versus solution gate voltage curve of a graphene device before GOx immobilization. The electrical measurement was done in the same condition with GNM device. The Dirac point of the graphene device shifted slightly to negative direction upon addition of glucose, which is similar with GNM without GOx function. Figure 2-7 (b) shows conductance versus solution gate voltage after the GOx immobilization process. The electrical characteristics behaved the same as none function sample, indicating little GOx has been successfully immobilized to the device.

In conclusion, we demonstrate an effective glucose sensor and pH sensor based on GNM device. We covalently linked GOx onto GNM. Dirac point of GOx functioned GNM device shift to the positive direction with increasing glucose concentration. Conductance of GOx functioned GNM increases selectively with introduction of glucose solution at solution gate voltage $-0.4V$. Conductance of GNM device increases stepwise with increasing pH, which is interpreted as electrostatic gating effect. This study highlights the promising potential of GNM in chemical functionalization and sensor application.

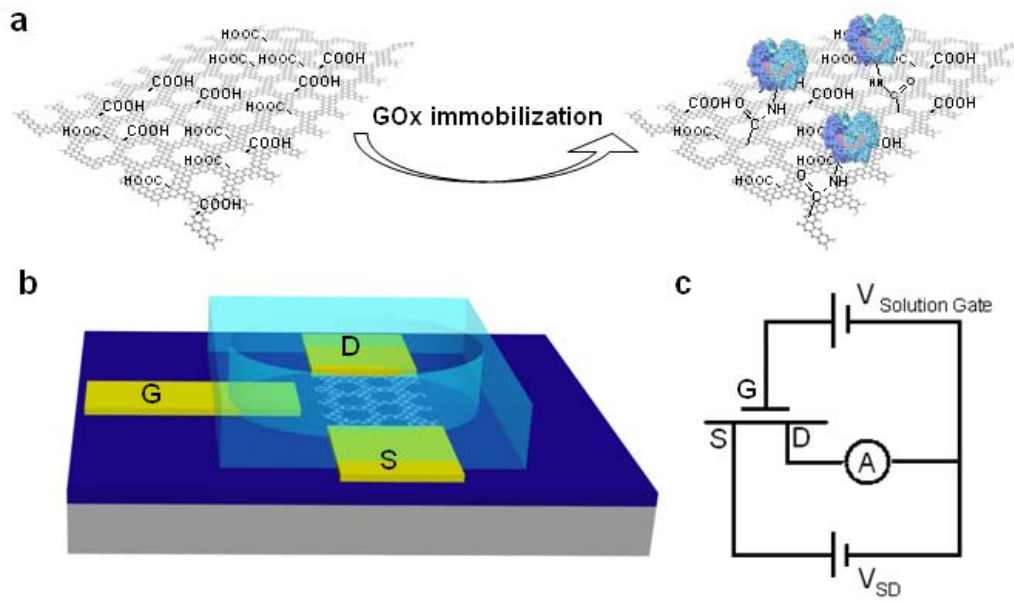


Figure 2-1. (a) Schematic illustration of GOx immobilization onto graphene nanomesh. (b) Schematic illustration of the sensor device layout. (c) Circuit diagram of electrical measurement system.

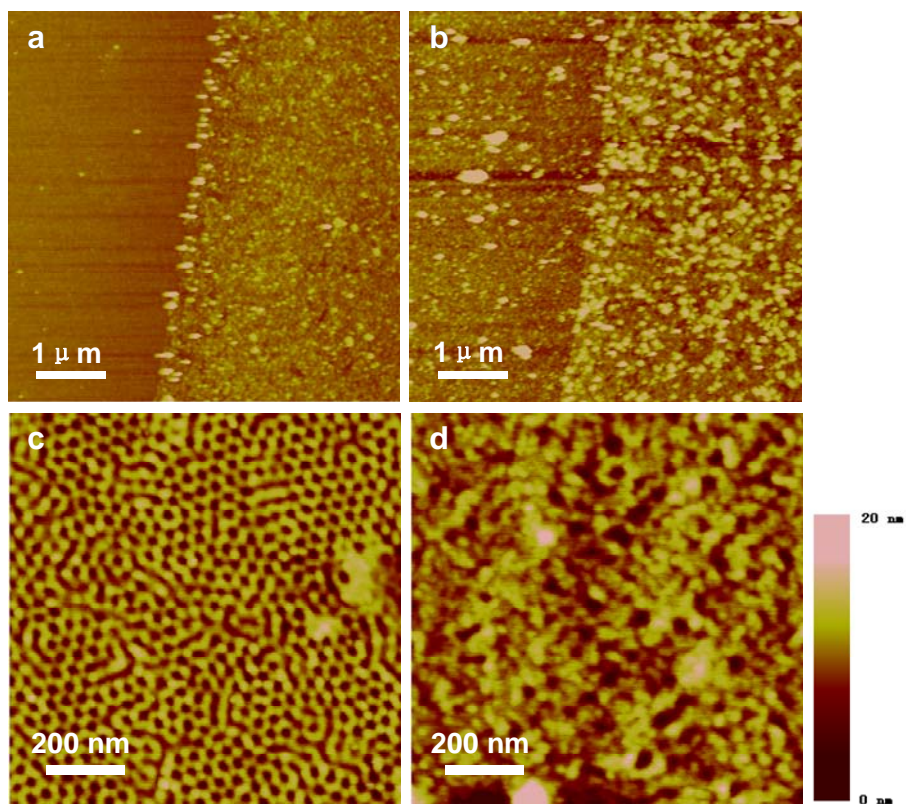


Figure 2-2 (a) and (c) AFM height image of GNM before GOx immobilization. (b) and (d) Enlarged AFM height image of GNM after GOx immobilization.

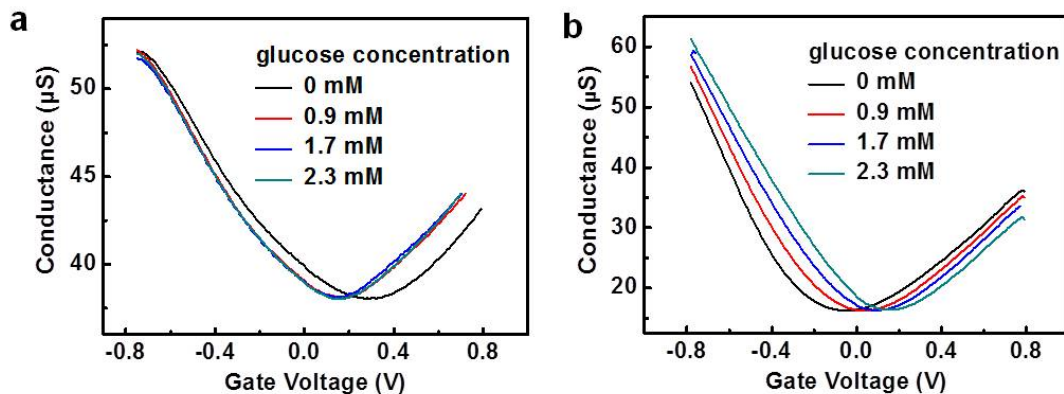


Figure 2-3. (a) Conductance of GNM as a function of solution gate voltage in glucose solution. (b) Conductance of GOx immobilized GNM as a function of solution gate voltage in glucose solution.

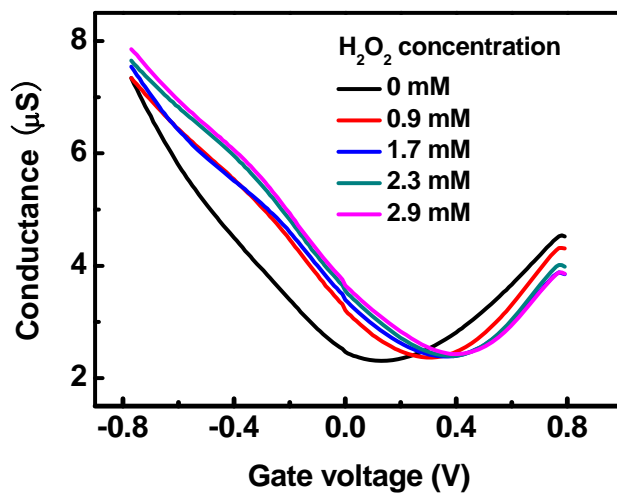


Figure 2-4 Conductance as a function of solution gate voltage of GOx immobilized GNM in different concentration H_2O_2 solution

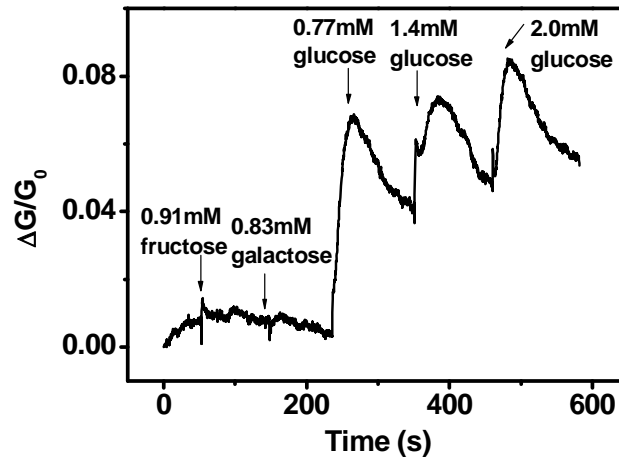


Figure 2-5. Real time electronic response of GNM glucose sensor. $\Delta G = G - G_0$. G is the conductance. G_0 means conductance at time = 0.

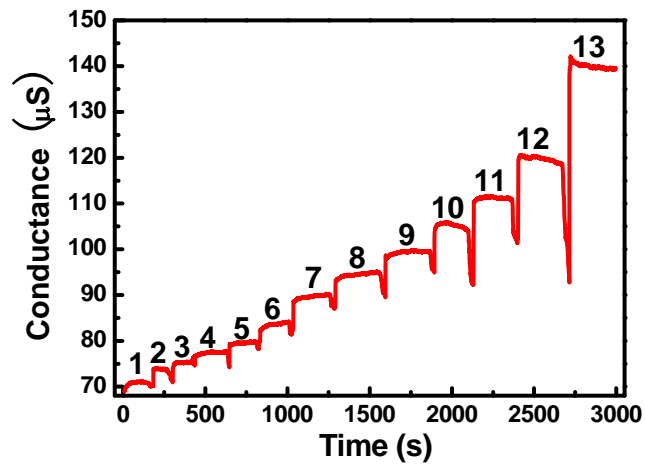


Figure 2-6 Conductance versus time of GNM for pH from 1 to 13.

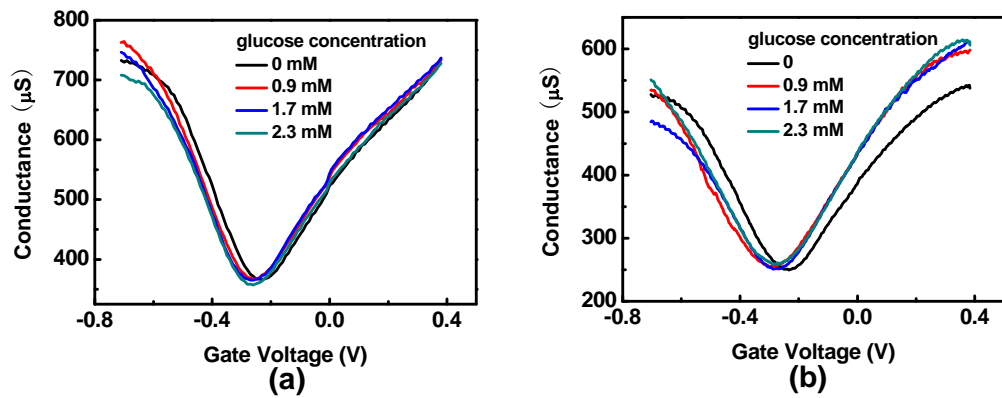


Figure 2-7. (a) Conductance as a function of solution gate voltage of Graphene device in glucose solution (b) Conductance as a function of solution gate voltage of GOx immobilized graphene device in glucose solution

Chapter III: REAL-TIME ELECTRICAL DETECTION OF NITRIC OXIDE IN BIOLOGICAL SYSTEMS WITH SUBNANOMOLAR SENSITIVITY

Real-time monitoring of nitric oxide concentrations is of central importance for probing the diverse roles of nitric oxide in neurotransmission, cardiovascular systems, and immune responses. In this chapter, we demonstrate a new design of nitric oxide sensors based on hemin functionalized graphene field-effect transistors. With its single atomic thickness and the highest carrier mobility among all materials, graphene holds the promise for unprecedented sensitivity for molecular sensing. The non-covalent functionalization through π - π stacking interaction allows reliable immobilization of hemin molecules on graphene without damaging the graphene lattice to ensure the highly sensitive and specific detection of nitric oxide. Our studies demonstrate that the graphene-hemin sensors can respond rapidly to nitric oxide in physiological environments with a sub-nanomolar sensitivity. Furthermore, *in vitro* studies show that the graphene-hemin sensors can be used for the detection of nitric oxide released from macrophage cells and endothelial cells, demonstrating their practical functionality in complex biological systems.

Nitric oxide (NO) is believed to play diverse and vital roles in neurotransmission, cardiovascular systems, and immune responses^{66,67}. Since NO was first discovered as an elusive endothelial-derived relaxing factor in 1987, extensive research efforts have been devoted to studying the function of NO in physiology and pathology⁶⁸⁻⁷⁰. To comprehensively understand the physiological roles of NO and to design new strategies to manipulate NO regulatory pathways for therapeutic purposes, it is desirable to probe

the production and diffusion processes of NO in biological systems in real-time. To this end, the reliable and specific detection of NO with high spatiotemporal resolution is essential. However, the accurate determination of NO concentration is of significant challenge because of its low concentration (nanomolar scale) and relatively short half life time (6-50s) in biological systems^{71,72}. Indirect detection methods — which rely on sensing secondary species such as nitrite and nitrate — are inherently ineffective for real-time detection. A number of direct detection methods such as electron paramagnetic resonance (EPR) spectroscopy, chemiluminescence, mass spectrometry and fluorescence⁷³⁻⁷⁵ are being developed for NO detection in biological systems. However, most of these methods either suffer from low sensitivity or require complicated sample preparation or measurement conditions that preclude real-time detection⁷².

Electrochemical NO sensing electrodes allow for real-time detection of NO with high sensitivity and selectivity⁷⁶⁻⁷⁹. However, as the signal amplitude and sensitivity of electrochemical sensors are generally proportional to the electroactive surface area of the electrodes⁷⁸, it is often difficult to simultaneously achieve high sensitivity and high spatial resolution. Electrochemical NO sensing electrodes with low nanomolar detection limit usually require an active area of 1500-30,000 μm^2 (refs. 72,78,79), and therefore cannot be used for high spatial resolution measurements of NO distribution at a single cell level, which is essential for the understanding of the signal transduction mechanisms of NO in physiology. Additionally, electrochemical NO sensors usually operate at a relatively high potential (typically > 0.6 V) for the electrochemical oxidation or reduction of NO to occur, which can disturb the intrinsic cellular response or induce significant signal interferences from other electrochemically active molecular species. The

application of a coating of NO selective gas permeable membrane on the electrode can improve the selectivity toward NO. However, greater selectivity usually requires thicker membrane, which not only complicates the fabrication process, but also lowers the sensitivity and retards the response speed⁷.

With specific molecular functionalization, solid-state semiconductor (e.g. GaAs) based field-effect transistors (FETs) can be configured as NO sensors with reduced dimension for real-time detection of NO in physiological solutions⁸⁰. However, the sensitivity of such sensors reported to date is typically limited to the micromolar regime, unsuitable for practical monitoring of biological NO levels that are typically in the nanomolar regime. Nanostructured materials are of increasing interest for the development of highly sensitive chemical and biological sensors^{81,82}. For example, with the unique single atomic thickness and exceptional electrical properties^{31,32}, graphene has recently received considerable attention for this purpose³³⁻³⁶.

Here we demonstrate the construction of hemin functionalized graphene FET as a new NO sensing device for highly sensitive and selective detection of NO in physiological conditions. With the single atomic thickness and the highest carrier mobility of all known materials, graphene-based NO sensors hold the promise for exceptional sensitivity that is not possible with other conventional materials for real-time, direct electrical readout of NO signals. We show that the graphene-hemin sensors can rapidly and selectively respond to NO in physiological solutions with a sub-nanomolar sensitivity, and can be used for real time monitoring of NO released from macrophage cells and endothelial cells, demonstrating their practical functionality in complex biological systems.

A. Experimental methods

Fabrication of graphene-hemin sensors.

Graphene was prepared by mechanical exfoliation onto a silicon substrate with a 300-nm thermal oxide layer. Titanium-gold thin film source, drain and solution gate electrodes were fabricated using e-beam lithography, vacuum metal deposition, followed by a lift-off process. A typical graphene FET device has an active channel area ranging from 0.5×0.5 to $0.5 \times 2 \mu\text{m}^2$, which is coupled with a polydimethylsiloxane (PDMS) microfluidic channel (with 0.5 mm channel height, 1 mm channel width and 10 mm channel length) for sample delivery (Fig. 3-1a).

The graphene FET was non-covalently functionalized with hemin chloride through the π - π stacking interaction to form an NO sensor (Fig. 3-1b)⁸³. The graphene devices were immersed in a 1 mg/mL hemin chloride/dimethyl sulfoxide (DMSO) solution for 2 hours to allow the non-covalent functionalization via π - π stacking. The sample was rinsed by DMSO for 3 times and isopropyl alcohol (IPA) for 3 times to wash away the unattached hemin molecules. After rinsing with IPA, the sample was blown dry with nitrogen gas. Hemin is chosen as the functionalization molecule due to its large binding constant and high selectivity towards NO⁸⁴. The non-covalent π - π interaction allows for the functionalization without damaging the graphene lattice or degrading its electronic performance.

Characterization of graphene-hemin sensors

UV-Vis absorption spectroscopy is used to characterize the immobilization of hemin molecules on graphene (Fig. 3-2a). Prior to hemin functionalization, graphene on quartz only shows expected nearly flat absorption around 2.3% in the visible range (black line in Fig. 3-2a). After hemin molecules are conjugated with graphene, a clear absorption peak is observed at 425 nm (red line in Fig. 3-2a), close to the Soret band of hemin. The control sample with free hemin in dimethyl sulfoxide (DMSO) solution exhibits an absorption peak at 403 nm (blue line in Fig. 3-2a). The red shift of the Soret absorption peak can be attributed to the π - π interaction between graphene and hemin, which rotates the ethylene groups to the coplanar conformation with the porphyrin ring and flattens the hemin molecule to enhance the π conjugation⁸⁵. We have quantified the amount of hemin molecules absorbed on graphene to be 0.94-hemin molecule/nm², nearly a complete monolayer of hemin on graphene (Fig. 3-3).

To calculate the surface concentration, UV-vis spectrum of hemin/DMSO (0.8 μ M) solution was measured (Fig. 3-3a, black curve). A sample of graphene on quartz was then immersed in the hemin/DMSO solution for 2 hours to let hemin absorb onto graphene. After taking the graphene sample out, the UV-vis spectrum of the hemin/DMSO solution is measured again (Fig 3-3a, red curve). The absorbance of hemin solution decreased after the functionalization process. The reduced absorbance can be attributed to hemin absorbed onto graphene. The surface concentration of hemin can be calculated using:

$$S_{\text{hemin}} = N_{\text{hemin}} / S_{\text{graphene}}$$

Where S_{hemin} is the surface concentration of hemin on the device, N_{hemin} is the total number of hemin on graphene, S_{graphene} is the total area of graphene, which is 0.90

cm² here. N_{hemin} can be calculated by subtracting the number of hemin remaining in the solution after functionalization from original hemin number.

$$N_{\text{hemin}} = N_{\text{hemin0}} - N_{\text{hemin1}} = (C_{\text{hemin0}} - C_{\text{hemin1}}) \times V$$

C_{hemin0} is the concentration of hemin in the DMSO solution before the functionalization (0.80 μM), C_{hemin1} is the concentration of hemin after the functionalization, which can be calculated with the absorbance and the calibration curve (Fig. 3-3b). The fitting equation of Fig. 3-3b is:

$$A = 0.220 \times C - 0.0015$$

So C_{hemin1} can be calculated through:

$$C_{\text{hemin1}} = \frac{A_{\text{hemin1}} + 0.0015}{0.220} = \frac{0.144 + 0.0015}{0.220} = 0.66 \mu M$$

So there is:

$$N_{\text{hemin}} = (C_{\text{hemin0}} - C_{\text{hemin1}}) \times V = (0.80 - 0.66) \mu M \times 1 \text{ mL} = 1.4 \times 10^{-10} \text{ mol}$$

$$S_{\text{hemin}} = \frac{N_{\text{hemin}}}{S_{\text{graphene}}} = \frac{1.4 \times 10^{-10} \text{ mol} \times 6.02 \times 10^{23} \text{ mol}^{-1}}{0.90 \text{ cm}^2} = 0.94 \text{ nm}^{-2}$$

So the surface density of hemin is about 0.94 molecule per square nanometer. As the size of hemin molecule is about 1×1 nm², the result is consistent with the formation of monolayer of hemin molecule on graphene.

This result of one monolayer is different from what reported in our previous paper⁸³, which can be attributed to different graphene materials used in these two different studies. The graphene used in the current study is obtained from mechanically

exfoliation or chemical vapor deposition (CVD), typically with a nearly perfect extended π -conjugation throughout the entire surface. As a result, the hemin molecules may interact with the graphene sample to form a nearly complete monolayer. In contrast, the reduced graphene oxide (rGO) was used in previous study⁸³. The rGO typically has a large number of epoxy, hydroxyl or carboxylic groups. With these defects and various functional groups, the large π -system is partially broken and the π - π interaction between hemin and rGO is weakened. The negatively charged carboxylic groups on graphene could also pose an electrostatic repulsion to hemin molecules (also with negatively charged carboxylic groups), to further weaken the interaction between rGO and hemin, particularly near the defective sites. As a result, the hemin molecules cannot conjugate with rGO as effectively as exfoliated or CVD graphene, to result in a lower coverage.

Atomic force microscope (AFM) is also used to characterize the hemin functionalized graphene. To this end, *e*-beam lithography is used to open up a 3 μm wide window, where graphene is selectively functionalized with hemin. The graphene sample was first protected with a layer PMMA and a window was opened using *e*-beam lithography, and then immersed into hemin/methanol solution for 2 hours. The sample was then taken out and rinsed with methanol and IPA, respectively. The sample was subsequently immersed in acetone and rinsed with IPA to remove the *e*-beam resist. Here methanol was used as the solvent to prevent the dissolution of *e*-beam resist PMMA by DMSO. The sensors functionalized in methanol solution respond to NO the same way as those functionalized in DMSO solution (Fig. 3-4). AFM image of the selectively functionalized graphene shows that the functionalized area exhibits a clear height

difference of ~ 0.5 nm from the un-functionalized area (Fig. 3-2b), which can be attributed to the formation of a monolayer of hemin molecules on graphene.

Raman spectroscopy is used to further characterize the immobilization of hemin molecules on graphene (Fig. 3-2c). The Raman spectrum of bare graphene (black line) shows two main peaks: the G band (1582 cm^{-1}) and the 2D band (2700 cm^{-1}), characteristic of graphene⁸⁶. After hemin functionalization, several new bands are observed at 1370 cm^{-1} , 1631 cm^{-1} , 1430 cm^{-1} , and 1307 cm^{-1} (red line), which can be assigned for ν_4 , ν_{10} , ν_{28} , and ν_{21} vibrational modes of hemin molecules, respectively⁸⁷. A decrease of the 2D band intensity is also observed after hemin immobilization. It was reported that the intensity of the 2D band decreases as a result of the interaction between graphene with either electron donating or electron accepting molecules⁸⁸. As a control experiment, a graphene sample is processed in DMSO (the solvent) without hemin through the same procedures of functionalization (blue line). No apparent change is observed in Raman spectrum compared to the bare graphene prior to processing, further supporting that the new Raman features (red line) observed in hemin–graphene conjugate indeed originate from the immobilized hemin on graphene rather than any other processing induced effects. Hence, these studies clearly demonstrate that hemin molecules are successfully immobilized on graphene.

NO solution preparation.

NO solution was prepared by dissolving an NO precursor (diethylamine NONOate sodium salt) into 10 mM NaOH solution followed by dilution with 10 mM phosphate buffered saline (PBS) (pH=7.4), following a protocol developed in previous NO sensor studies⁸⁰. All NaOH and PBS solutions were pre-bubbled with N_2 for 2 hours

to remove the dissolved oxygen. Diethylamine NONOate sodium salt was added to a 10 mM NaOH solution to make a stock solution of 500 μ M. Serial dilution was performed with the stock solution and 10 mM PBS (pH=7.4) to make NO solutions of various concentrations. The NO-containing PBS solutions were allowed to set for at least 15 minutes before the introduction into the PDMS channel to allow the NO concentrations to saturate. Griess test was used to confirm the concentration of NO generated by diethylamine NONOate (Fig. 3-5).

Electrical measurement.

The electrical transport measurements were conducted with a Lakeshore probe station (Model TTP4) and a computer-controlled analogue-to-digital converter (National Instruments model 6030E). All the sensing measurements were carried out under ambient conditions, with a pre-deposited Ti-Au pad as solution gate electrode.

B. Results and discussion

Real-time electrical detection of NO.

We then tested the electrical responses of graphene devices to NO solutions in real time. All the following real-time electrical measurements were conducted at a constant bias voltage of 10 mV and solution gate of 0 V unless otherwise stated. The leakage current through the solution gate is typically less than 3 nA (Fig. 3-6), which is negligible compared to the typical source drain current of the graphene-hemin devices ($\sim 1\mu$ A). Two devices on the same substrate were kept in a PDMS well filled with 10 mM phosphate buffered saline (PBS) (pH=7.4), with only one of the devices selectively functionalized with hemin (setup as Fig. 3-7). Both devices exhibited positive Dirac

points with p-type characteristics at 0 V solution gate voltage bias (hole-transport branch). We used diethylamine NONOate sodium as a precursor to release NO in PBS solution (pH=7.4)⁸⁹⁻⁹¹. At neutral pH, each one of these precursor molecules can hydrolyze to generate two molecules of NO, following a first order reaction kinetics with a half lifetime of ~2 minutes⁸⁹. At basic pH (pH \geq 12), this hydrolysis reaction proceeds much more slowly and is nearly negligible compared to that at neutral pH. Two devices were tested in parallel. With the introduction of 0.2 μ L of a 10 mM NaOH aqueous solution (Fig. 3-2d, point A) or 0.2 μ L of the precursor/PBS solution, in which NO had been eliminated by 2 hours of N₂ bubbling (Fig. 3-2d, point B), neither device showed any obvious conductance change. In contrast, upon the introduction of 0.2 μ L of a 100 μ M diethylamine NONOate sodium in NaOH solution into the PBS in the PDMS well (Fig. 3-2d, point C), the hydrolysis generation of NO is initiated at neutral PH value, the conductance of hemin functionalized device exhibits a noticeable gradual drop (Fig. 3-2d, red line). The time-dependent conductance response curve gives a half lifetime of ~135 seconds, consistent with the hydrolysis kinetics expected for the NO precursor at pH 7.4 (ref. 89). On the other hand, the un-functionalized device does not show any obvious conductance change because there is no active sites for NO binding (Fig. 3-2d, black line). This study clearly demonstrates that hemin functionalized graphene device can indeed respond specifically to NO in PBS solutions.

We have further determined the sensitivity of the graphene-hemin NO sensors. To this end, the NO sensing experiments were performed using a micro-fluidic system with a PDMS channel integrated on top of the graphene device (Fig. 3-1a), with which the freshly prepared NO solutions of increasing concentrations were introduced into the

PDMS channel through a syringe pump. Figure 3-8a shows a real-time electrical readout of different concentrations of NO from 0 to 1000 nM. The average response time of the steps ($t_{90\%}$) is about 2 seconds, largely limited by the diffusion at the interface of different concentrations of NO sample solutions.

At the interface of different concentration NO, the diffusion length L_D can be calculated using:

$$L_D = 2 \times \sqrt{D \times t}$$

Where D is the diffusion constant of NO in aqueous solution, which is $\sim 1.0 \times 10^{-5} \text{ mm}^2/\text{s}$, t is the time of diffusion. Here t is the time for the solution to travel from the bottle to the device through the tube.

$$t = 240 \text{ s}$$

$$L_D = 2 \times \sqrt{D \times t} = 2 \times \sqrt{1.0 \times 10^{-5} \text{ mm}^2 \cdot \text{s}^{-1} \times 240 \text{ s}} = 0.098 \text{ mm}$$

So the length of the interface in between two different concentration NO solutions is 0.098 mm. The diameter of the tube is 0.762 mm. The cross-sectional area of the tube is 0.456 mm^2 . The time required for this interface diffusion length to pass through the device (t') is:

$$t' = L_D \times S \div q = 0.098 \text{ mm} \times 0.456 \text{ mm}^2 \div (100 \mu\text{L} \cdot \text{h}^{-1}) = 1.6 \text{ s}$$

Limited by this diffusion time, the apparent response time of our device is around 1.6 s, even though the intrinsic response of the device might be faster.

The inherent response time of the sensor is likely to be much faster. To obtain the calibration curve for NO detection, the amount of the conductance change was plotted against NO concentration (Fig. 3-8b). The calibration curve in Fig. 3-8b can be fitted with a logarithmic plot. At low NO background concentration (e.g. $< 10 \text{ nM}$), a lowest

absolute detection limit of 0.3 nM can be achieved with a signal to noise ratio of 3. With increasing background NO concentration, the absolute sensitivity is reduced. Nonetheless, a relative sensitivity of 3-10 % (the percentage of the concentration variation over the background concentration) is maintained consistently even at the highest NO concentration due to the nature of logarithmic relationship. Since the conductance change of the sensor originates from the doping effect, it is expected that the sensor devices with higher transconductance (g_m) should exhibit higher sensitivity. Indeed, the detection limits of different devices show a consistent trend with a lower detection limit achieved in the device with higher transconductance (Fig. 3-8c). Together, these studies clearly demonstrate that the graphene-hemin devices can function as highly sensitive sensors for the detection of NO molecules in PBS solutions.

To better understand the effect of NO on the electrical properties of the sensor device, the conductance of the device was plotted against solution gate voltage in PBS with different NO concentrations (Fig. 3-8d). The hemin immobilized graphene devices show a consistent negative shift of the Dirac point with increasing NO concentration from 0 to 1000 nM. This negative shift of the Dirac point can be attributed to the doping effect of the hemin complex to the graphene channel upon the binding of NO to the Fe(III) center. Specifically, with the immobilization of hemin onto graphene, the Fe(III) center in hemin can interact with graphene in a metal-ligand model, similar to the Fe(III) benzene complexes⁹². In this case, graphene donates π -electrons to the d-orbital of Fe(III) through a cation- π interaction. When NO molecules come to coordinate with and donate electrons to Fe(III) centers, those π -electrons are partially transferred back to the valence band of graphene due to the trans effect of the ligands⁹³. Therefore, the binding of NO to Fe(III)

centers is equivalent to partial electron-doping to hemin-functionalized graphene. This electron-doping effect explains the negative shifting of the Dirac point upon the introduction of NO, and is consistent with the reduction of conductance in the hole-transport branch of the graphene devices. Importantly, when monitoring the graphene-hemin device in electron-transport branch, a conductance increase is observed upon the introduction of NO (Fig. 3-9), consistent with the electron-donating nature of the NO binding events.

Raman spectroscopy study was also used to characterize the graphene-hemin device in the PBS solution of NO (Fig. 3-8e). The G-band is found to shift to lower frequencies when the NO concentration is increased, consistent with n-type doping to graphene by electron donating molecules reported in literature⁸⁸. On the other hand, the G-band of bare graphene does not exhibit any significant shift of frequency with the increasing NO concentration (Fig. 3-10). It is also important to note that the Raman shift is rather small, and only noticeable at relatively high NO concentrations (>100 nM), while the electrical signal is detectable at a much lower concentration of NO down to 1 nM or less.

Selectivity and functionality in physiological solutions.

We have further investigated the selectivity and specificity of the graphene-hemin devices as NO sensors. With the introduction of a series of potentially interfering chemicals including oxygen, hydrogen peroxide, sodium nitrate, sodium nitrite, L-citrulline, L-arginine, and diethylamine NONOate sodium bubbled with N₂ (which contains only the hydrolyzed precursor but not NO), no obvious conductance change is observed (Fig. 3-11a). In contrast, a conductance drop is clearly observed with the

addition of 1 nM NO, demonstrating the excellent selectivity of our graphene-hemin NO sensors. We have also tested additional potentially interfering chemicals including l-glutathione, sodium ascorbate, carbon monoxide, hydrogen sulfide, sodium thiocyanate, and sodium cyanide with the same devices (Fig 3-11b). At the same concentration of 100 nM, the device responds to NO with the strongest signal, demonstrating excellent selectivity of our device to NO.

To further demonstrate the practical functionality of the sensor in physiological solutions, we have also conducted the NO sensing measurements in Dulbecco's modified eagle medium (DMEM). The DMEM solution is a typical cell culture medium, containing various kinds of proteins, amino acids, vitamins, inorganic salts and other compounds including glucose. Furthermore, we have also tested the sensor performance in real biological samples such as fetal bovine serum that contains a large variety of potentially interfering species at physiological levels. In both cases, stepwise responses are clearly observed from the NO sensor when different NO concentrations are introduced (Fig. 3-11c, d). Importantly, the detection limits of 0.4 nM and 1.4 nM were achieved in DMEM solution (see calibration curve shown in Fig. 3-12a) and fetal bovine serum (see calibration curve shown in Fig. 3-12b), respectively, demonstrating the proper functionality of our sensors in physiological solutions.

We have also evaluated the stability of the graphene-hemin sensors by measuring the sensitivity of the same device after 1 week and 3 weeks of storage under ambient conditions (Fig. 3-13). The sensitivity of the sensor is 54 $\mu\text{S}/1000\text{ nM}$ originally, and became 53 $\mu\text{S}/1000\text{ nM}$ (98%) after 1 week, 47 $\mu\text{S}/1000\text{ nM}$ (89%) after 3 weeks, which are comparable with the electrochemical sensors^{7,12}. This signal drift is likely due to non-

specific surface adsorptions, and the stability of the device may be further improved through storage in a controlled environment.

Real-time monitoring of NO released by living cells.

Going a step further, we have also conducted *in vitro* studies to test the performance of the graphene-hemin NO sensors for real-time detection of extracellular NO generated from RAW 264.7 macrophage cells. It is well known that macrophage cells can generate NO with expression of inducible nitric oxide synthase (iNOS) when stimulated by lipopolysaccharide (LPS)⁹²⁻⁹⁷. RAW 264.7 cells were obtained from the American Type Culture Collection (ATCC, Manassas, VA) and cultured in Dulbecco's modified eagle medium (DMEM; Carlsbad, CA) containing 10 % fetal calf serum (FCS), 100 U/mL penicillin, 100 µg/mL streptomycin, and 2 mM L-glutamine (complete medium). These cells were maintained in 25 cm² cell culture flasks, in which the cells were passaged at 70~80% confluency every 2~4 days. RAW 264.7 cells were seeded at 5×10^5 cells per mL (cell suspension) onto the graphene-hemin device on the SiO₂ substrate (inset, Fig. 3-14b) within a PDMS well (setup as Fig. 3-7). The cells were cultured for 12 hours at 37 °C in a 5% CO₂ incubator before NO sensing measurement. The sensing measurement was carried out at 37 °C.

As shown in Fig. 3-14a (A), after LPS (100 ng/mL) was introduced (at $t = 1$ h), the conductance of graphene-hemin device exhibited a gradual decrease, corresponding to an increase of NO concentration (Fig. 3-14b(A)). The NO concentration reached a maximum around $t = 6$ h and remained stable for the following 5 hours, followed by a slow decrease. This time course is consistent with the expected kinetics of NO generation by iNOS in macrophage cells⁹²⁻⁹⁶. In contrast, when LPS (100 ng/mL) and

aminoguanidine (AG, an iNOS inhibitor) (100 μ M) were added together, the change of conductance was almost negligible (Fig. 3-14a (B)). The conductance of the control device without LPS stimulation remained as the same value during the measurement (Fig. 3-14a (C)). As shown in Figure 5b, the conductance of the device was converted to NO concentration by using the calibration curve of the graphene-hemin device (Fig. 3-15, red curve). In general, the time response and overall concentration of NO are within the expected ranges for NO generated by macrophage cells. Moreover, the standard Griess test was also used to test NO released by the same batch of RAW 264.7 macrophage cells (Fig. 3-16), which shows a consistent time course with that obtained from the electrical measurements. These results clearly demonstrate that the graphene-hemin sensors are capable of the real-time monitoring of extracellular NO generated from RAW 264.7 macrophage cells over a period of 20 hours. Importantly, the calibration curve of the same device after the 20 hours of continuous NO measurement shows that the sensitivity of the sensor is largely retained (Fig. 3-15), further demonstrating the excellent long-term stability of the sensor.

The time dependent NO concentrations measured by the Griess test (Fig. 3-16) and the electrical measurement (Fig. 3-14a) are apparently different. The difference comes from different detection mechanism. In brief, our NO sensor measures real time NO concentration (that is being generated by the cells and oxidized into NO_2^- simultaneously), and the Griess test measures the accumulated amount of NO_2^- . In RAW 264.7 cells, iNOS catalyzes the oxidation of L-arg to generate NO after LPS stimulation. As the L-Arg is consumed, its concentration gets lower, and the generation of NO gets slower. At the same time, NO is rapidly oxidized by oxygen in the solution to generate

NO_2^- . It has been reported previously that depletion of L-Arg triggers O_2^- (radical anion) generation from iNOS. O_2^- oxidizes NO to form the potent oxidant peroxynitrite (ONOO^-), which leads to even faster consumption of NO. The real-time profile of the NO concentration shows a period of increasing NO concentration, followed by a steady state and a decrease of NO concentration, which is consistent with the above generation and oxidation consumption mechanism. On the other hand, Griess test measures the final oxidation product (NO_2^-), which is continuously generated by the reaction of NO and O_2 , and accumulated in the solution. That is why Griess assay shows continuous signal increase. A trend of saturation can be observed after 15 hours (Fig. 3-16c), which is consistent with the time when NO concentration starts to decrease in real-time measurement by our sensor (Fig. 3-14a).

We have further explored our sensor for the real time detection of NO released from endothelial cells (ECs). The production of nitric oxide (NO) by vascular endothelial cells plays an important role in normal vascular physiology⁹⁸⁻¹⁰⁰. Endothelial-derived NO can account for inhibition of platelet aggregation and adhesion and for the modulation of vascular tone. Direct measurement of NO released from endothelial cells is difficult because NO is generated in small amounts and degrades fast in biological system. Importantly, we show that the graphene-hemin sensor can be readily used to measure NO released by human umbilical vein endothelial cells (HUVECs). Human umbilical vein endothelial cells (HUVECs) were obtained from the ATCC and cultured in F-12K Medium (ATCC, Manassas, VA) supplemented with 10 % FCS, 0.1 mg/mL heparin; 0.05 mg/mL endothelial cell growth supplement (ECGS). These cells were maintained in 25 cm^2 cell culture flasks, in which the cells were passaged at 70~80% confluency every 5

days. The HUVECs were seeded at 5×10^5 cells/mL (cell suspension) onto the graphene-hemin device on the SiO₂ substrate (inset, Fig. 3-14d) within a PDMS well (setup as in Fig. 3-7). HUVECs were cultured for 12 hours at 37 °C in a 5% CO₂ incubator before the NO sensing measurement.

The sensing measurement was carried out at 37 °C. With the introduction of bradykinin (20 nM) (which serves as an agonist to stimulate the NO generation) at $t=120$ s, the conductance of graphene-hemin device started to decrease almost instantly (Fig. 3-14c (A)), and reached a plateau after about 150 s. The conductance then kept constant for about 600 s before a gradual increase to almost the original value in about another 200 s. As a control experiment, HUVECs were cultured with culture media with 1 mM L-NG-nitroarginine methyl ester (L-NAME), an eNOS inhibitor, for 1 hour before the electrical measurement. When bradykinin was added to the control sample, no apparent change of conductance was observed (Fig. 3-14c (B)). The conductance of another control device without bradykinin stimulation kept constant during the measurement (Fig. 3-14c (C)). Using the calibration curve of this graphene-hemin device (Fig. 3-17), the conductance of the device can be converted to NO concentration (Fig. 3-14d). The concentration of NO started to increase after the injection of bradykinin and reached a plateau of ~ 20 nM in 150 s (Fig. 3-14d (A)). The time course and the concentration of NO are within the expected ranges of NO released by endothelial nitric oxide synthase (eNOS)⁹⁸⁻¹⁰⁰. These studies further demonstrate the capability of the graphene-hemin sensors to detect not only large amount of NO over a long period of time, but also nanomolar range NO with fast response in complex biological systems.

In brief, we have reported a new design of graphene-hemin FET based NO sensor for direct electrical readout of NO signals in real time . Unlike electrochemical sensors, the fundamental sensitivities of our graphene NO sensors are not directly dependent on their sizes. It can therefore allow us to scale the sizes of the sensors down to the lithographic limit while retaining a high sensitivity. Importantly, our study demonstrates sub-nanomolar detection limit (0.3 nM) can be achieved in submicron graphene-hemin sensors ($0.25 \mu\text{m}^2$), which can only be achieved in electrochemical sensors at least 4-5 orders of magnitude larger ($1,500\text{-}30,000 \mu\text{m}^2$). Considering the two-dimensional nature of graphene materials, the miniaturized graphene NO sensor array can be readily integrated over large area for high spatial resolution detection and imaging of NO signal. Additionally, our graphene hemin NO sensors can operate at a much lower bias voltage (e.g., 10 mV) than the working potential of electrochemical NO sensors (e.g., $> 0.6 \text{ V}$), and is therefore less invasive to biological systems.

We have shown that the tested NO sensors can exhibit high sensitivity in physiological solutions such as cell culture media or real biological samples such as fetal bovine serum, and can be used for the real time monitoring of NO released by macrophage cells and endothelial cells. All these samples represent complex real biological conditions with a large number of potentially interfering species at physiological levels. Together, these studies clearly demonstrate that our sensors can be used to detect NO in complex biological samples with excellent sensitivity, selectivity, as well as a rapid response speed. Along with their miniaturized sizes, these graphene-hemin NO sensors are promising as a new platform for highly sensitive real-time monitoring of NO signals in biological system with high spatiotemporal resolution.

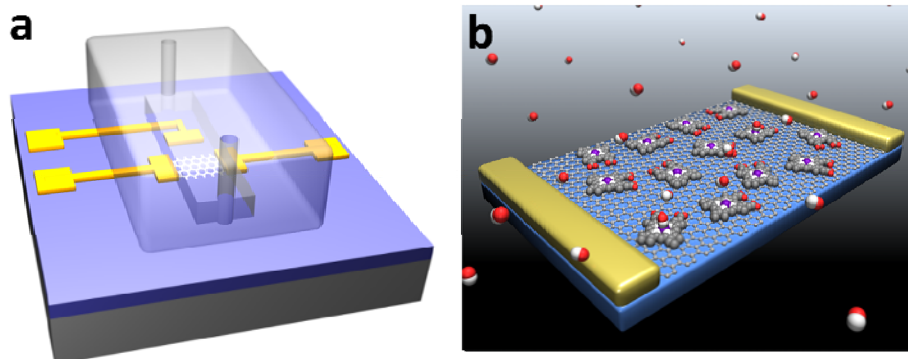


Figure 3-1 | Schematic illustration of a graphene-hemin conjugate device. (a) Schematic of a graphene device with integrated micro-fluidic sample delivery system. A typical graphene device has an active area of 0.5×0.5 to $0.5 \times 2 \mu\text{m}^2$, and sizes of source and drain electrodes are $2 \times 5 \mu\text{m}^2$ (excluding the electrical leads), and the size of gate electrode is $50 \times 50 \mu\text{m}^2$. The micro-fluidic polydimethylsiloxane (PDMS) channel has a width of 1 mm, height of 0.5 mm and length of 1 cm. **(b)** Schematic illustration of graphene-hemin conjugate.

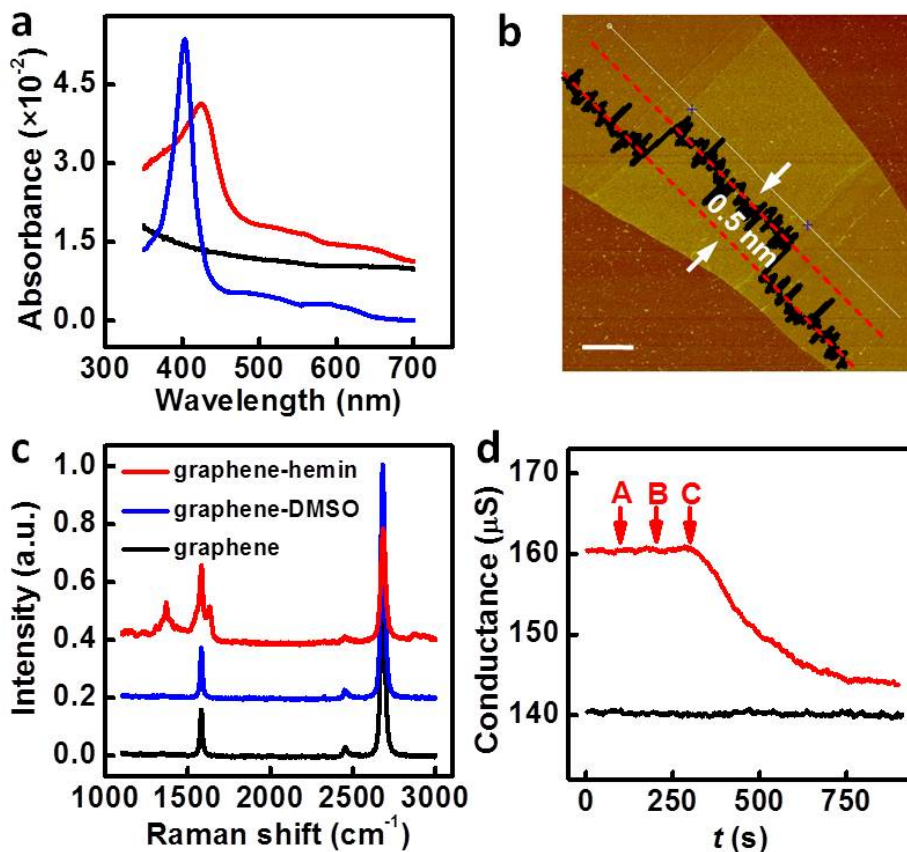


Figure 3-2 | Characterization of graphene-hemin conjugate. (a) UV-Vis spectrum of graphene before and after hemin immobilization. Black: bare graphene; red: graphene after immersed in hemin DMSO solution, blue: hemin in DMSO solution. (b) AFM image of graphene after hemin immobilization. The scale bar is 1 μm . (c) Raman spectra of graphene before and after hemin functionalization. Black: bare graphene; blue: graphene after immersed in DMSO, with an offset of 0.2; red: graphene-hemin conjugate, with an offset of 0.4. (d) Real-time electrical measurement with nitric oxide precursor solution directly added onto graphene-hemin device inside a polydimethylsiloxane (PDMS) well filled with PBS solution. Graphene-hemin device (red) and bare graphene

device (black) were measured in parallel within the same PDMS well. Solution A is 0.01 M NaOH. B is NO precursor in PBS bubbled with N₂ for 2 hours (essentially the same as C, but with NO removed). C is NO precursor in NaOH solution (Both B and C are 1 μM after diluted in the PDMS well).

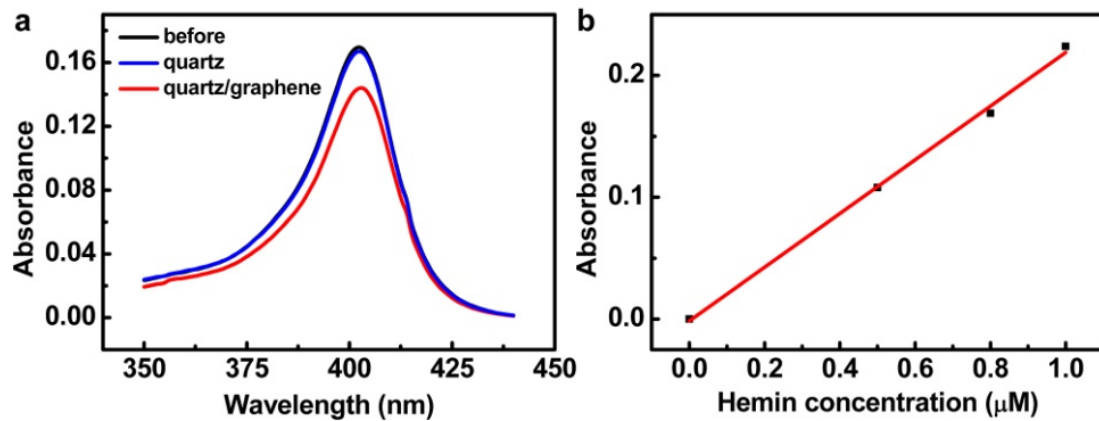


Figure 3-3 | Determination of surface coverage of hemin on graphene. (a) UV-Vis spectrum of hemin DMSO solution before (black) and after reaction with quartz substrate (blue) and quartz with graphene (red). (b) The UV-Vis absorbance calibration curve for hemin DMSO solution.

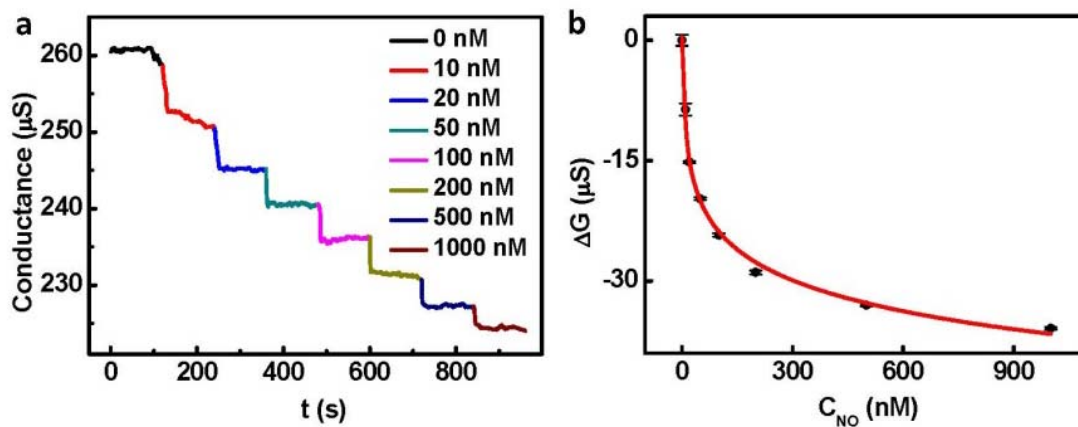


Figure 3-4 | Real-time electrical readout of NO signal by graphene-hemin sensor functionalized in hemin/methanol solution. (a) Real-time electrical measurement at different concentrations of NO. (b) Calibration curve: conductance change versus NO concentration. The red line is the fitted curve in natural log scale.

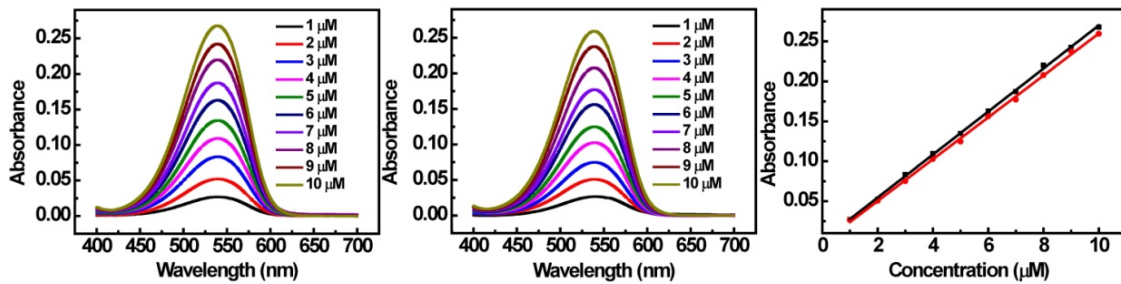


Figure 3-5 | NO released by diethylamine NONOate measured with Griess test. (a) UV-Vis spectrum of NO_2^- at different concentration. (b) UV-Vis spectrum of NO generated by diethylamine NONOate at different concentration. (c) Calibration curve of absorbance v.s. concentration. black line: NO_2^- ; red line: NO generated by diethylamine NONOate.

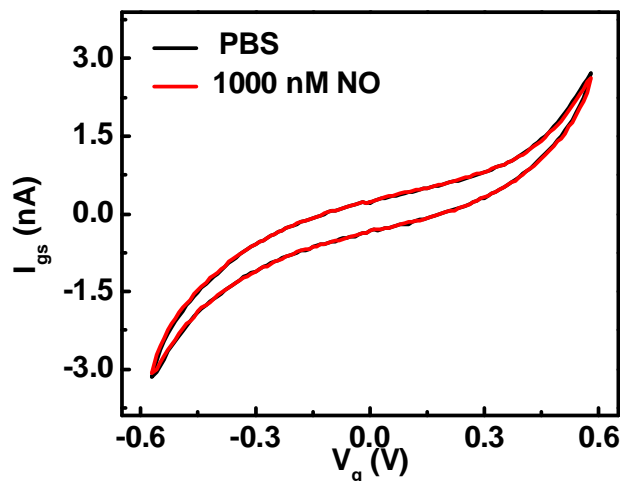


Figure 3-6 | Leakage current between gate electrode and source electrode in PBS and 1000 nM NO.

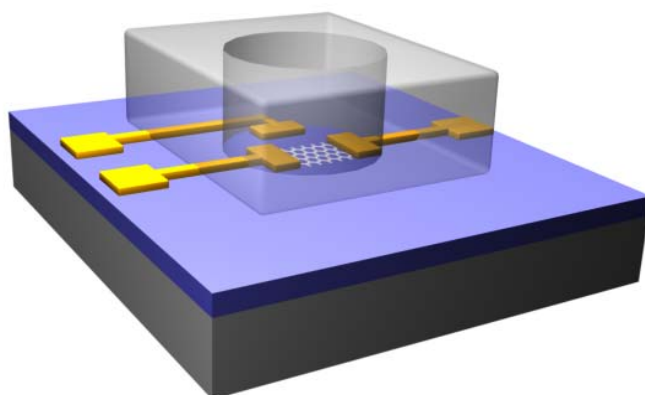


Figure 3-7 | Schematic illustration of graphene-hemin device in PDMS well (3 mm in diameter, 5 mm in depth).

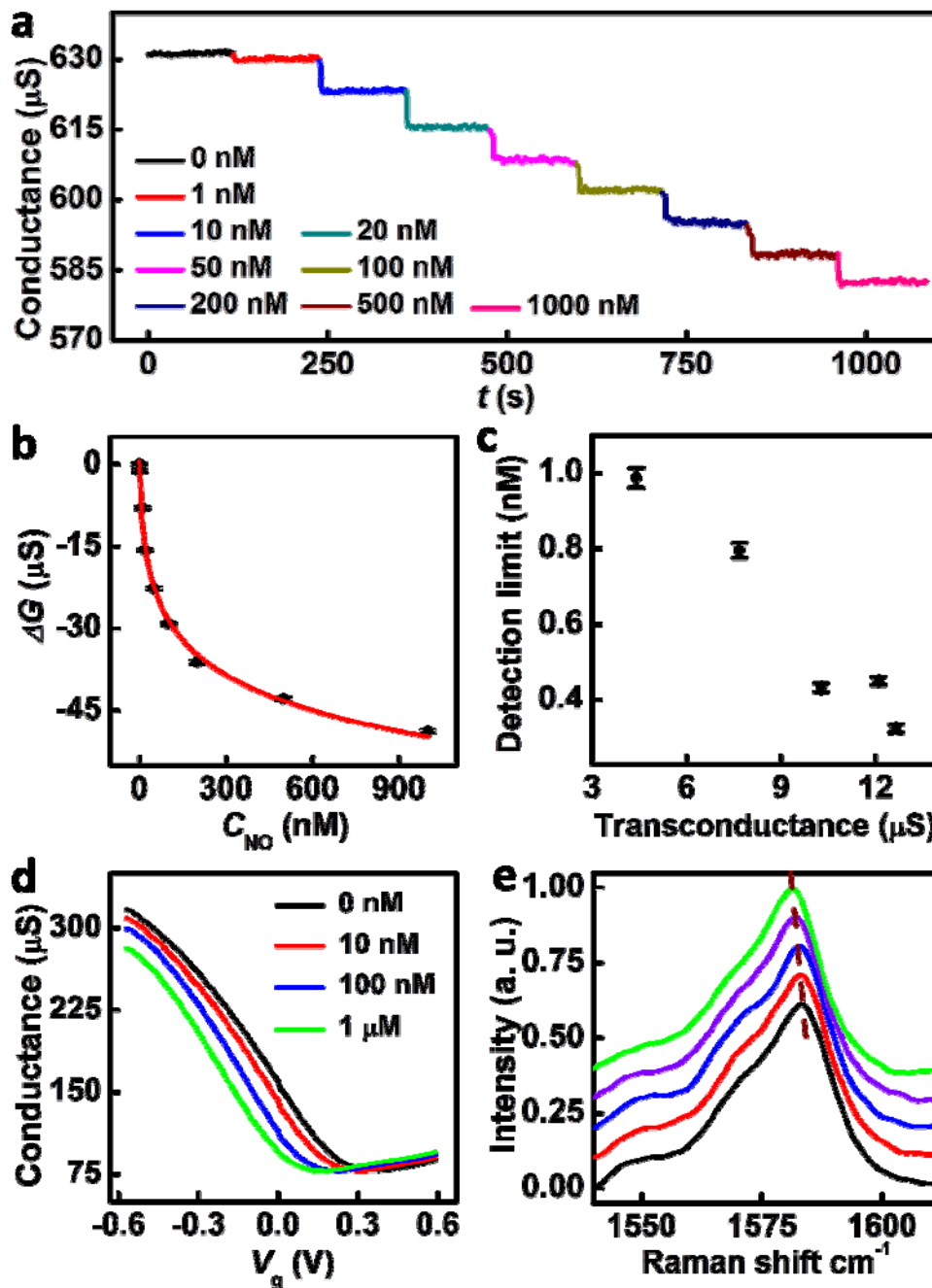


Figure 3-8 | Real-time electrical readout of NO signals. (a) Real-time electrical measurement of different concentrations of NO. (b) Calibration curve: conductance change (ΔG) versus NO concentration (C_{NO}). The red line is the fitted curve in natural logarithmic scale. (c) Relationship of the detection limit v.s. the transconductance of

different sensor devices. (d) Solution gate dependent measurement at different concentrations of NO. V_g stands for solution gate voltage. (e) Raman spectra of graphene-hemin in different concentration NO solution. Black: PBS; red: 100 nM NO, with 0.1 offset; blue: 1 μ M NO, with 0.2 offset; violet: 10 μ M NO, with 0.3 offset; green: 100 μ M NO, with 0.4 offset.

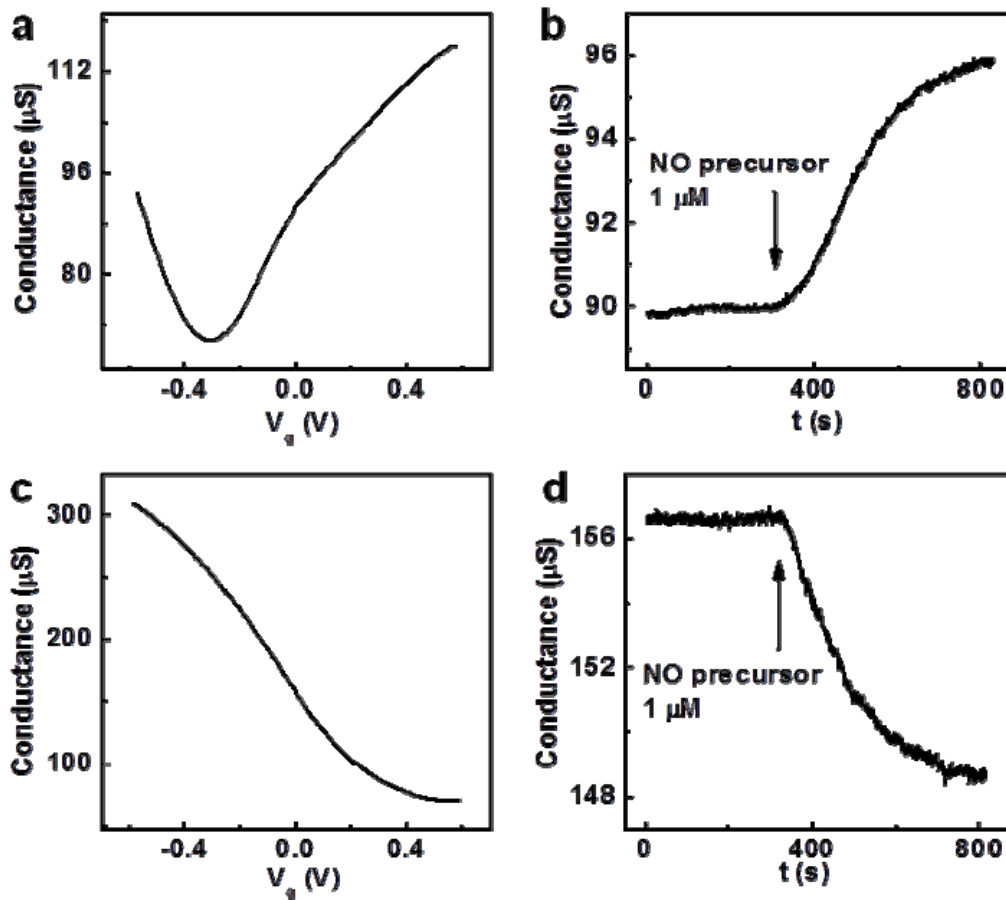


Figure 3-9 | Electrical measurement NO detection with both p- and n-graphene-hemin device. (a), (b) are measured with device 1 (n-type); (c), (d) are measured with device 2 (p-type). (a) Solution gate dependent measurement of device 1. (b) Real-time measurement of graphene-hemin device 1 with the introduction of NO precursor (1 μ M) at 0 solution gate. (c) Solution gate dependent measurement of device 2. (d) Real-time

measurement of graphene-hemin device 2 with the introduction of NO precursor ($1 \mu\text{M}$) at 0 solution gate.

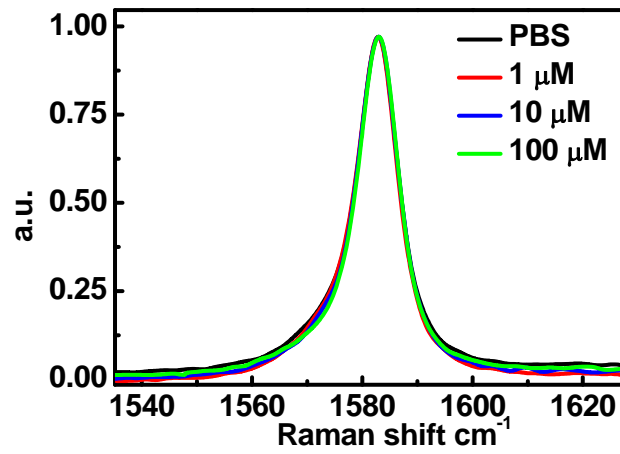


Figure 3-10 | Raman spectra of bare graphene in variable concentration NO solution.

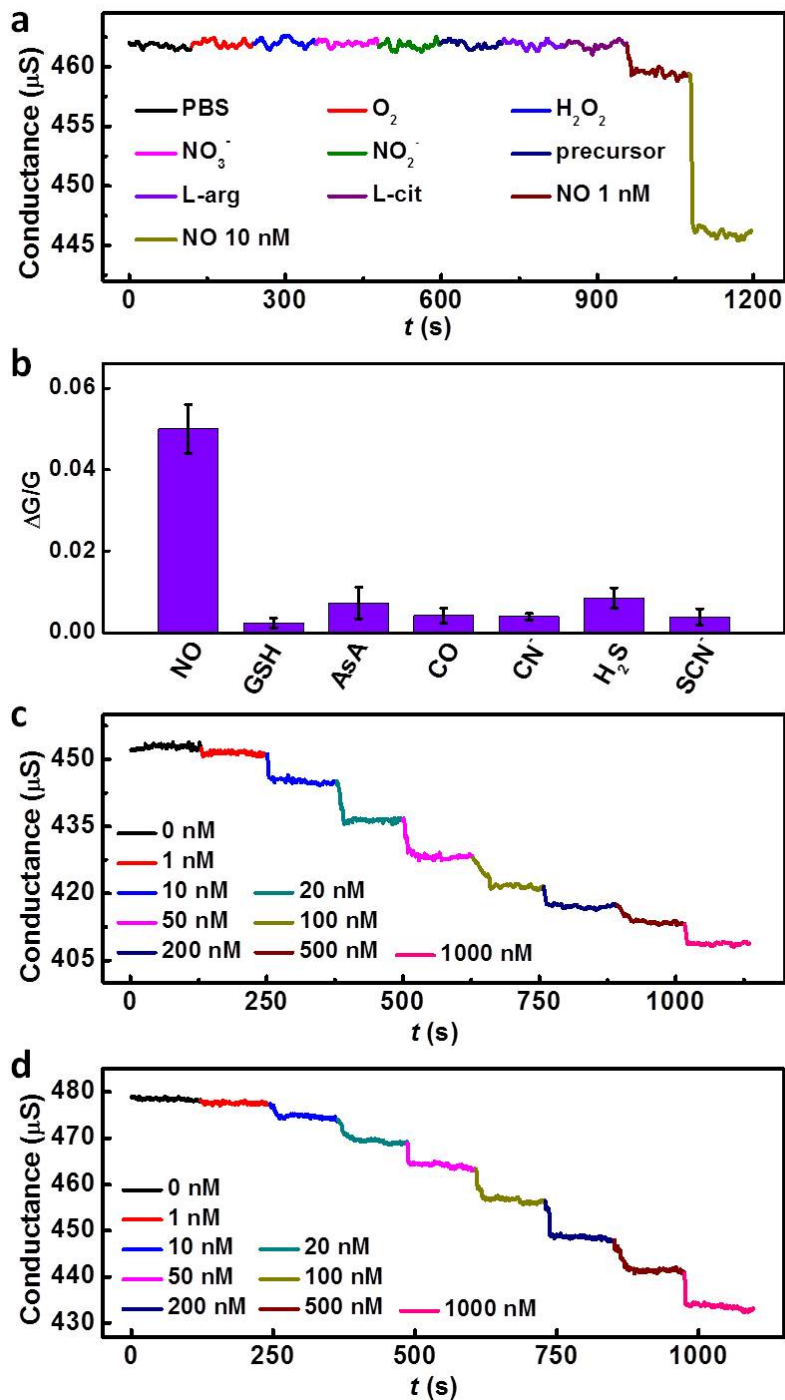


Figure 3-11 | Selectivity and practical functionality in physiological solutions. (a) Selectivity measurement with the addition of a series of control solutions (1 M) followed by NO solutions (1 nM and 10 nM). (b) Selectivity measurement with NO and

potentially interfering chemicals (all chemicals have a concentration of 100 nM, GSH stands for l-glutathione, Asc stands for sodium ascorbate). Signal is defined by $\Delta G/G$, where ΔG is the conductance change and G is the conductance. The signals are the averages of 3 devices. (c) Real-time electrical measurement at different concentrations of NO in Dulbecco's modified eagle medium (DMEM). (d) Real-time electrical measurement at different concentrations of NO in fetal bovine serum.

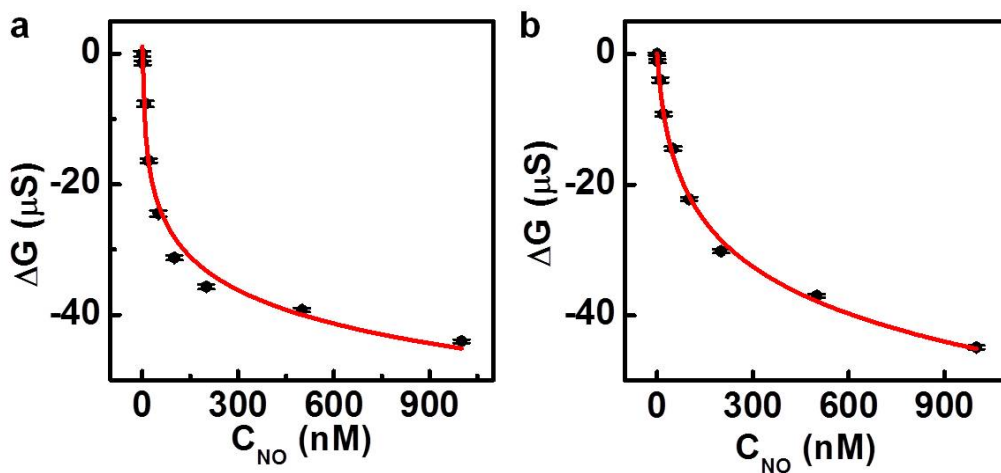


Figure 3-12 | Calibration curve in DMEM and fetal bovine serum. (a) Calibration curve in DMEM. (b) Calibration curve in fetal bovine serum.

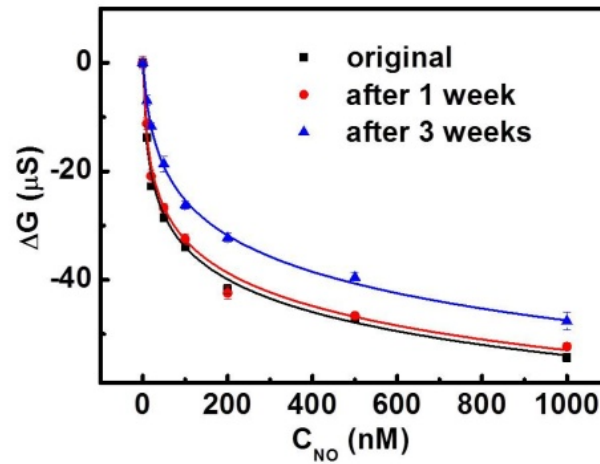


Figure 3-13 | The sensitivity of a same device after 1 week and 3 week storage in ambient environment. The sensitivity of the sensor is $54 \mu\text{S}/1000 \text{ nM}$ originally, $53 \mu\text{S}/1000 \text{ nM}$ (98%) after 1 week, $47 \mu\text{S}/1000 \text{ nM}$ (89%) after 3 weeks.

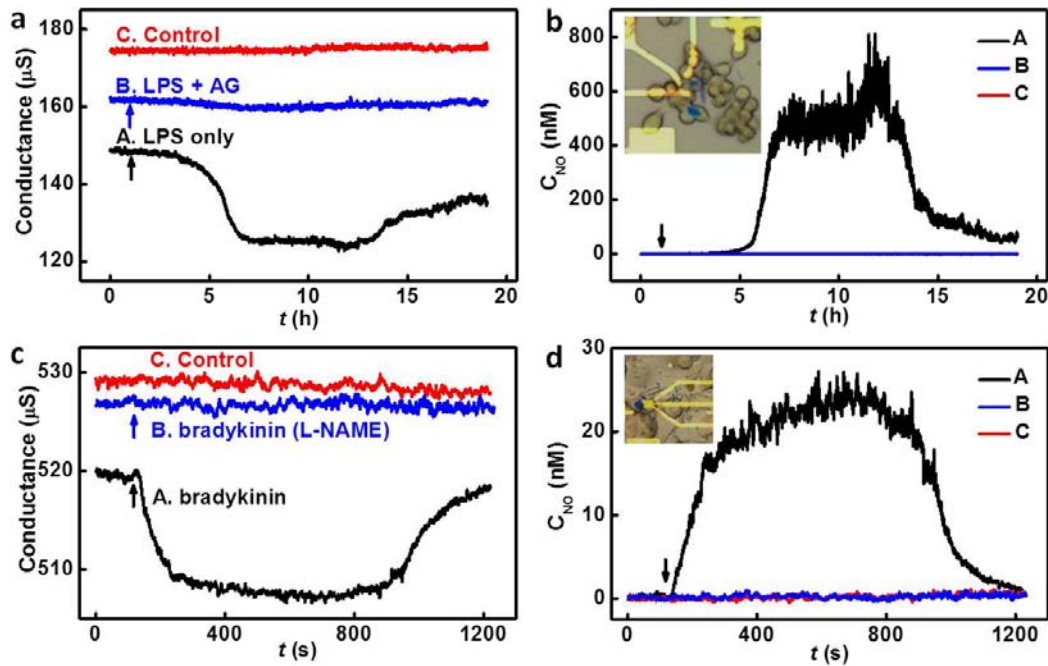


Figure 3-14 | **Real-time detection of NO released from living cells.** (a) and (b): Real-time monitoring of NO released from Raw 264.7 macrophage cells. (a) Real-time

measurement of the conductance of the sensor device for NO detection. **(b)** Real-time measurement of the NO concentration. Inset: Optical microscope image of RAW 264.7 cells seeded on the graphene-hemin device. In both **(a)** and **(b)**: (A) 100 ng/mL LPS, (B) 100 ng/mL LPS and 100 μ M AG, (C) without LPS. **(c)** and **(d)**: Real-time monitoring of NO released from human umbilical vein endothelial cells (HUVECs). **(c)** Real-time measurement of the conductance of the sensor device. **(d)** Real-time measurement of the NO concentration. Inset: Optical microscope image of HUVECs seeded on the graphene-hemin device. In both **(c)** and **(d)**: (A) 20 nM bradykinin, (B) 20 nM bradykinin and 1 mM L-NAME, (C) without bradykinin.

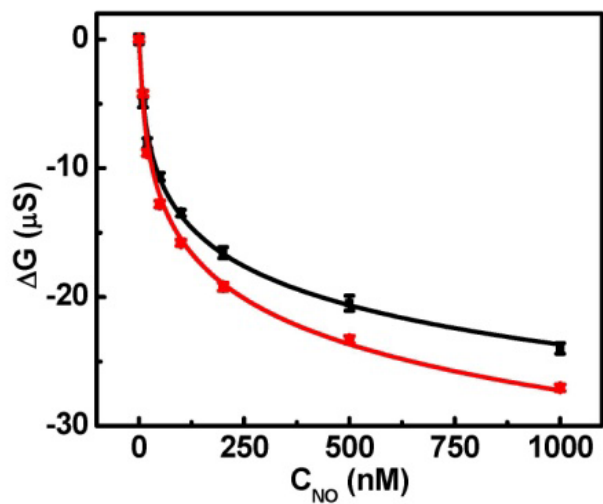


Figure 3-15 | Calibration curve in DMEM for the device before and after 20 hours of NO measurement with RAW 264.7 macrophage cells. Red: before the 20 hours of NO measurement; Black: after the NO measurement.

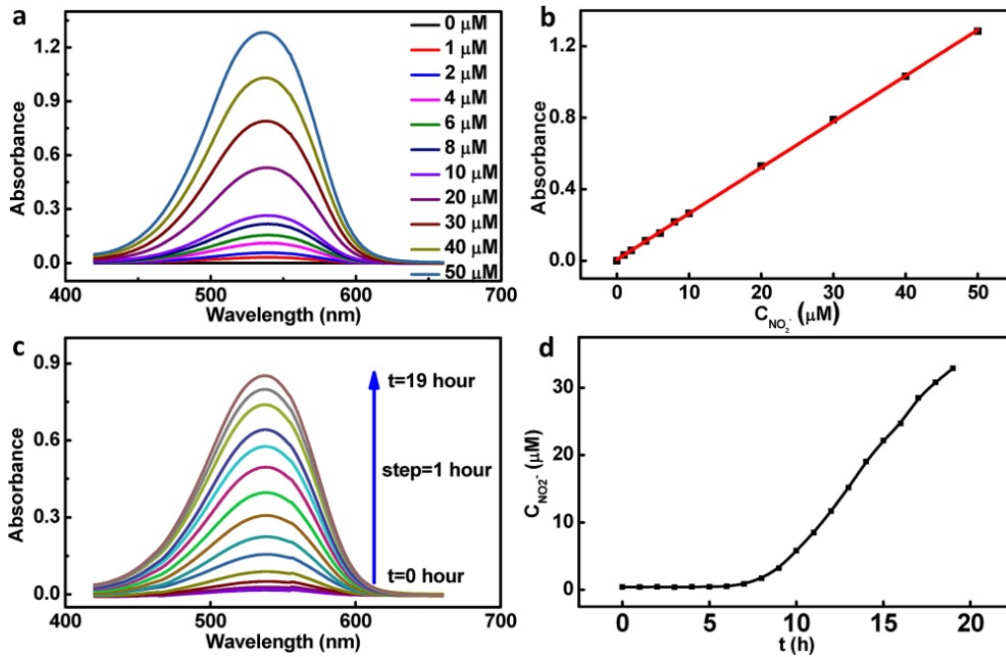


Figure 3-16 | NO released by RAW 264.7 macrophage cells measured with Griess test. (a) UV-Vis spectrum of NO_2^- at different concentration. (b) Calibration curve of peak absorbance of NO_2^- at different concentration. (c) UV-Vis spectrum of RAW 264.7 cells culture media at different time with LPS stimulation at $t = 1\text{h}$. (d) Time dependent NO_2^- concentration in RAW 264.7 cells culture media measured by UV-Vis spectrum, with LPS stimulation at $t = 1\text{h}$.

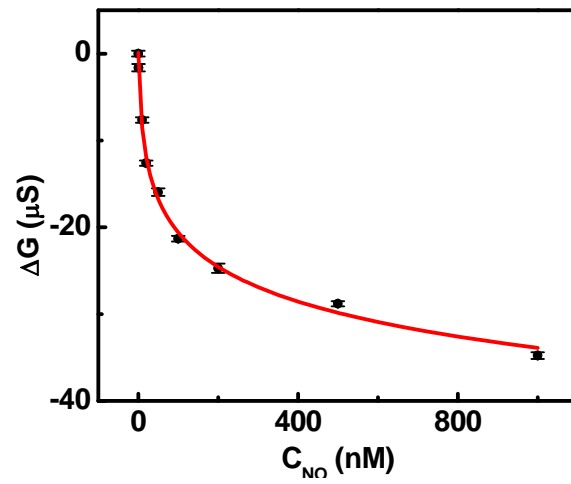


Figure 3-17 | Calibration curve in DMEM for the device used in detection of NO generated from HUVECs.

Chapter IV: HIGHLY SENSITIVE MERCURY(II) SENSOR BASED ON THIN-LAYERED MOLYBDENUM DISULFIDE FIELD-EFFECT TRANSISTOR

Apart from graphene, other two-dimensional layered materials, such as MoS₂ and WSe₂, are also emerging as an exciting material system for a new generation of atomically thin electronic devices. With its ultrahigh surface to volume ratio and excellent electrical properties, few-layer MoS₂ holds the promise for unprecedented sensitivity for sensing application. The detection of mercury in aquatic environment is of great importance because mercury is an environment pollutant with severe toxicity. Here we report the construction of few-layer molybdenum disulfide (MoS₂) based field-effect transistor (FET) device for highly sensitive detection of Hg²⁺ ion in aquatic solutions. High binding affinity between mercury and sulfur makes MoS₂ a promising candidate for mercury sensing. Our studies demonstrate that MoS₂ sensors selectively respond to Hg²⁺ ion with a detection limit of 30 pM. This MoS₂ FET based mercury sensor promises great potential for highly sensitive, label-free, low-cost, fast and non-aggressive detection of mercury in aquatic environment.

The detection of mercury in aquatic environment is of great importance because it is one of the most toxic elements affecting human health¹⁰¹. Mercury contamination is an important environmental problem originating from anthropogenic sources such as coal and fuel combustion. According to the World Health Organization (WHO)'s standards, mercury concentration should be less than 0.001 mg/L (5 nM) in drinking water¹⁰². It is essential to develop highly sensitive mercury detection techniques to determine very low concentrations of mercury for reliable risk assessment¹⁰³⁻¹⁰⁷. Mercury (II) (Hg²⁺) is one of

the most usual and stable forms of mercury pollution in aquatic environment. Mercury (II) detection techniques including atomic absorption spectrometry, atomic fluorescence spectrometry, and inductively coupled plasma mass spectrometry have been intensively studied¹⁰². However, these detection methods are usually time consuming and require complicated sampling procedures which damage the integrity of the sample. On the other hand, electronic devices based sensors are favorable for portable, label free, non-aggressive and fast detection^{108,109}.

2D layered materials are very promising for chemical sensing application, because they have ultrahigh surface to volume ratio which makes their electrical properties extremely sensitive to the environment¹¹²⁻¹¹⁶. Here we report the construction of MoS₂ field-effect transistor (FET) device for highly sensitive detection of Hg²⁺ ion in aquatic solutions (Fig. 4-1a). Due to the high binding affinity between mercury and sulfur, Hg²⁺ ion can strongly bind to sulfur on the surface of MoS₂ and thus affect the electrical properties of the MoS₂ FET device. We show that the MoS₂ sensor can selectively respond to Hg²⁺ ion in real-time with a detection limit of 30 pM.

A. Experimental methods

Fabrication of MoS₂ mercury sensor

To fabricate the MoS₂ mercury sensor, few-layer MoS₂ flakes were prepared by mechanical exfoliation onto 300 nm Si/SiO₂ substrate. Electron-beam lithography and electron beam evaporation were used to define the contact electrodes. A thin Ni/Au film (5nm/50 nm) was used as the electrode to form Ohmic contact with minimized contact resistance and potential barrier. The MoS₂ device is then coupled with a polydimethylsiloxane (PDMS) microfluidic channel for sample delivery.

Measurement of the electrical properties of the MoS₂ device

We have first characterized the electrical transport properties of MoS₂ to ensure Ohmic contacts were achieved. To this end, the MoS₂ FETs were fabricated on Si/SiO₂ substrate, with Ni/Au thin film as the source-drain contacts, and the silicon substrate as a back gate electrodes. The I_{ds} - V_{ds} characteristics at varying back gate voltage (Fig. 4-2a) and the I_{ds} - V_{bg} characteristics (Fig. 4-2b) for MoS₂ were measured. Importantly, a linear I_{ds} - V_{ds} relationship is clearly observed, indicating Ohmic contacts are achieved. Furthermore, I_{ds} - V_{bg} plot shows that the current increases with increasing positive gate voltages for MoS₂, indicating an n-type semiconductor behavior.

B. Results and discussion

Sensitivity of the MoS₂ Hg²⁺ ion sensors

We have further determined the sensitivity of the MoS₂ Hg²⁺ ion sensors. To this end, the Hg²⁺ ion sensing experiments were performed using a micro-fluidic system with a PDMS channel integrated on top of the graphene device, with which the Hg²⁺ ion solutions of increasing concentrations were introduced into the PDMS channel through a syringe pump (Fig. 4-1a). Hg²⁺ ion solutions were made by dissolving Hg(ClO₄)₂ into phosphate buffered solution (pH=7.0). Figure 3a shows a real-time electrical readout of different concentrations of Hg²⁺ ion from 0 to 1 μ M. To obtain the calibration curve for Hg²⁺ ion detection, the amount of the conductance change was plotted against the Hg²⁺ ion concentration (Fig. 4-3b). The calibration curve in Fig. 3b can be fitted with a logarithmic plot. A lowest absolute detection limit of 30 pM can be achieved with a signal to noise ratio of 3.

Investigation of the sensing mechanism

To better understand the effect of Hg^{2+} ion on the electrical properties of the sensor device, the conductance of the device was plotted against solution gate voltage with different Hg^{2+} ion concentrations (Fig. 4-3c). The MoS_2 devices show a consistent negative shift of the threshold voltage with increasing Hg^{2+} ion concentration from 0 to 1 μM . This negative shift of the threshold voltage can be interpreted as a p-doping effect of the Hg^{2+} ion to the MoS_2 channel. The stability constant for Hg^{2+} ion coordination with a S^{2-} ligand is $10^{52.4}$. In this case, sulfur on the surface of MoS_2 donates electrons from its HOMO to the LUMO of Hg^{2+} ion, causing a p-doping effect to the MoS_2 FET.

To further study the doping effect from Hg^{2+} ion to MoS_2 , photoluminescence spectroscopy study was also used to characterize the MoS_2 device in the aqueous solution of Hg^{2+} ion (Fig. 4-4a-c). The peak energy of peak A is blue-shifted in Hg^{2+} ion solution as compared to that in deionized water (Fig. 4-4a). The spectral shape of peak A is also sharper in Hg^{2+} ion solution. Peak A can be decomposed into the exciton (X; ~ 1.88 eV; red line) peak and the negative trion (X^- ; ~ 1.84 eV; blue line) by Gaussian fit functions (Fig. 4-4b,c). The exciton peak X becomes more dominant in Hg^{2+} ion solution (Fig. 4-4c), indicating the excitons can recombine without forming trions because of the decrease of excess electrons in MoS_2 , suggesting p-doping effect by Hg^{2+} ion¹¹⁷. Also a broad shoulder peak (L; ~ 1.75 eV; yellow line) becomes much stronger in Hg^{2+} ion solution. As a bound exciton peak, L indicates additional binding sites available for excitons from the Hg-S interaction¹¹⁸.

Selectivity of the MoS_2 Hg^{2+} ion sensors

We have further investigated the selectivity and specificity of the MoS₂ devices as Hg²⁺ ion sensors (Fig. 4-5). We have also tested a series of potentially interfering chemicals including sodium (I), potassium (I), magnesium (II), calcium (II), manganese (II), iron (II), iron (III), cobalt (II), nickel (II), tin (II), lead (II), zinc (II), cadmium (II), silver (I) and copper (II). At the same concentration of 1 nM, the device responds to mercury with the strongest signal, demonstrating excellent selectivity of our device to mercury.

In brief, we have reported a new MoS₂ FET based mercury sensor for direct electrical readout of Hg²⁺ ion signals in real time . Picomolar detection limit (30 pM) of Hg²⁺ ion was achieved. The sensing mechanism is based on the strong binding affinity between Hg²⁺ ion and sulfur on the surface of MoS₂. The sensor also shows excellent specificity toward Hg²⁺ ion against a series of interferences. This novel mercury sensor promised great potential for highly sensitive, label-free, low-cost, fast and non-aggressive detection of mercury in aquatic environment.

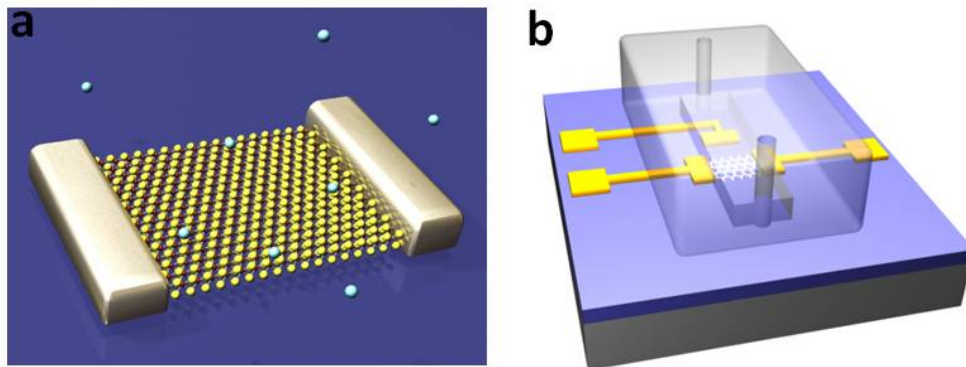


Figure 4-1| Schematic illustration of a MoS₂ Mercury (II) sensor. (a) Schematic illustration a MoS₂ device sensing Hg²⁺ ion. (b) Schematic of microfluidic measurement setup integrated with.

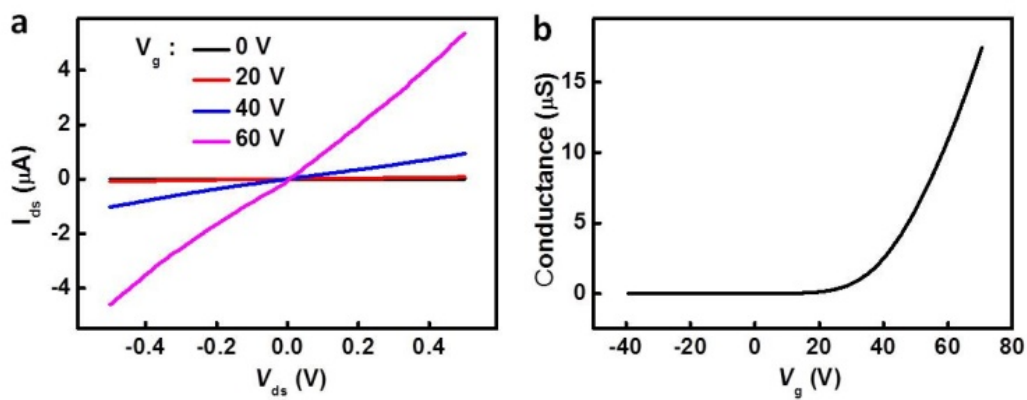


Figure 4-2| Electrical transport properties of a MoS₂ FET. (a) I_{ds} - V_{ds} characteristics at varying back gate voltage of a MoS₂ FET. (b) I_{ds} - V_{bg} characteristics of MoS₂ FET.

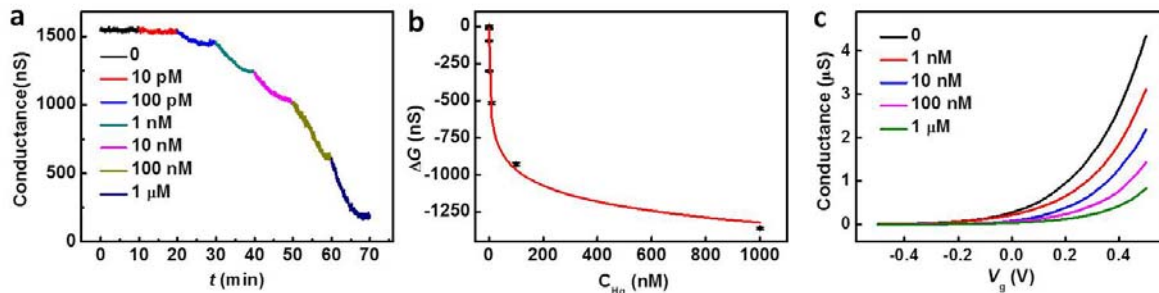


Figure 4-3| Real-time electrical readout of Hg²⁺ ion signal by MoS₂ sensor. (a) Real-time electrical measurement at different concentrations of Hg²⁺ ions. (b) Calibration curve: conductance change versus Hg²⁺ ion concentration. The red line is the fitted curve in natural log scale. (c) Solution gate dependent measurement at different concentrations of Hg²⁺ ion.

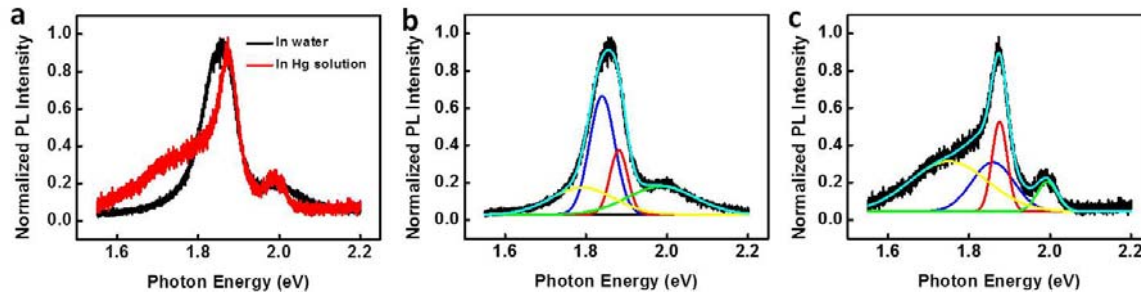


Figure 4-4| Photoluminescence spectroscopy of sensor in Hg²⁺ ion solution. (a) PL spectroscopy of few-layered MoS₂ in water and in Hg²⁺ ion solution. (b) Analysis of the PL spectroscopy for few-layered MoS₂. The A peak was reproduced by assuming two peaks with Lorentzian functions, corresponding to the trion (X⁻) and the exciton (X) peaks, were overlapped. (c) Analysis of the PL spectroscopy for few-layered MoS₂ in Hg²⁺ ion solution.

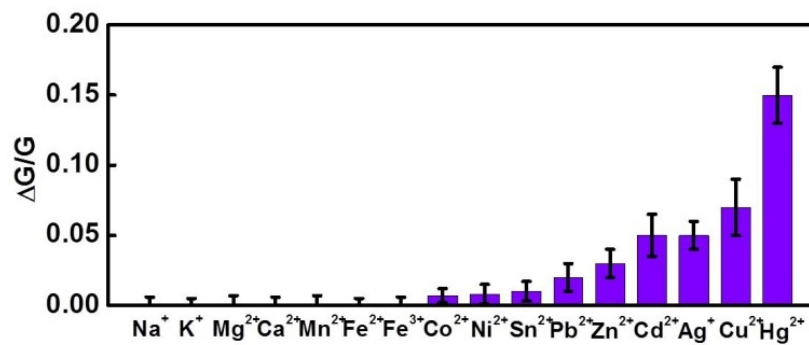


Figure 4-5| Selectivity of MoS₂ Mercury (II) sensor. Concentrations of Mercury (II) and all the interferences are 1 nM.

CONCLUSION

My doctoral research is focused on graphene electronic device based biosensors and chemical sensors. It contains three different research project. The first one is the fabrication of graphene nanomesh (GNM) and its application as glucose and pH sensor, in which we covalently linked glucose oxidase onto GNM, and detect glucose and pH change through conductance change. The study highlights the promising potential of GNM in chemical functionalization and sensor application. The second research project I did was real-time electrical detection of nitric oxide in biological systems with subnanomolar sensitivity. In brief, we created a new design of graphene-hemin FET based NO sensor for direct electrical readout of NO signals in real time. Our study demonstrates sub-nanomolar detection limit (0.3 nM) can be achieved in submicron graphene-hemin sensors ($0.25 \mu\text{m}^2$). Considering the two-dimensional nature of graphene materials, the miniaturized graphene NO sensor array can be readily integrated over large area for high spatial resolution detection and imaging of NO signal. We have shown that the tested NO sensors can exhibit high sensitivity in physiological solutions such as cell culture media or real biological samples such as fetal bovine serum, and can be used for the real time monitoring of NO released by macrophage cells and endothelial cells. Together, these studies clearly demonstrate that our sensors can be used to detect NO in complex biological samples with excellent sensitivity, selectivity, as well as a rapid response speed. Along with their miniaturized sizes, these graphene-hemin NO sensors are promising as a new platform for highly sensitive real-time monitoring of NO signals in biological system with high spatiotemporal resolution. The third research project was highly sensitive highly sensitive mercury (II) sensor based on thin-layered molybdenum

disulfide field-effect transistor. In brief, we constructed a new MoS₂ FET based mercury sensor for direct electrical readout of Hg²⁺ ion signals in real time . Picomolar detection limit (30 pM) of Hg²⁺ ion was achieved. The sensing mechanism is based on the strong binding affinity between Hg²⁺ ion and sulfur on the surface of MoS₂. The sensor also shows excellent specificity toward Hg²⁺ ion against a series of interferences. The results of my research represent a significant step forward to the development of highly sensitive, label-free, low-cost, fast and non-aggressive biosensors and chemical sensors.

REFERENCES

- [1] Castro Neto, A. H.; Guinea, F.; Peres, N. M. R.; Novoselov, K. S., and Geim, A. K., *Rev. Mod. Phys.* **81**, 109-162 (2009).
- [2] Novoselov, K. S.; Jiang, D.; Schedin, F.; Booth, T. J.; Khotkevich, V. V.; Morozov, S. V., and Geim, A. K., *P. Natl. Acad. Sci. USA* **102**, 10451-10453 (2005).
- [3] Blake, P.; Hill, E. W.; Neto, A. H. C.; Novoselov, K. S.; Jiang, D.; Yang, R.; Booth, T. J., and Geim, A. K., *Appl. Phys. Lett.* **91**, 063124 (2007).
- [4] Ni, Z. H.; Wang, H. M.; Kasim, J.; Fan, H. M.; Yu, T.; Wu, Y. H.; Feng, Y. P., and Shen, Z. X., *Nano Lett.* **7**, 2758-2763 (2007).
- [5] Bruna, M. and Borini, S., *Appl. Phys. Lett.* **94**, 031901 (2009).
- [6] Ferrari, A. C.; Meyer, J. C.; Scardaci, V.; Casiraghi, C.; Lazzeri, M.; Mauri, F.; Piscanec, S.; Jiang, D.; Novoselov, K. S.; Roth, S., and Geim, A. K., *Phys. Rev. Lett.* **97**, 187401 (2006).
- [7] Ferrari, A. C., *Solid State Commun.* **143**, 47-57 (2007).
- [8] Graf, D.; Molitor, F.; Ensslin, K.; Stampfer, C.; Jungen, A.; Hierold, C., and Wirtz, L., *Nano Lett.* **7**, 238-242 (2007).
- [9] Neto, A. H. C. and Guinea, F., *Phys. Rev. B* **75**, 045404 (2007).
- [10] Geim, A. K. and Novoselov, K. S., *Nat. Mater.* **6**, 183-191 (2007).
- [11] Novoselov, K. S.; Geim, A. K.; Morozov, S. V.; Jiang, D.; Zhang, Y.; Dubonos, S. V.; Grigorieva, I. V., and Firsov, A. A., *Science* **306**, 666-669 (2004).
- [12] Novoselov, K. S.; Geim, A. K.; Morozov, S. V.; Jiang, D.; Katsnelson, M. I.; Grigorieva, I. V.; Dubonos, S. V., and Firsov, A. A., *Nature* **438**, 197-200 (2005).

- [13] Bolotin, K. I.; Sikes, K. J.; Jiang, Z.; Klima, M.; Fudenberg, G.; Hone, J.; Kim, P., and Stormer, H. L., *Solid State Commun.* **146**, 351-355 (2008).
- [14] Zhang, T.; Clowes, S. K.; Debnath, M.; Bennett, A.; Roberts, C.; Harris, J. J.; Stradling, R. A.; Cohen, L. F.; Lyford, T., and Fewster, P. F., *Appl. Phys. Lett.* **84**, 4463-4465 (2004).
- [15] Gilbertson, A. M.; Branford, W. R.; Fearn, M.; Buckle, L.; Buckle, P. D.; Ashley, T., and Cohen, L. F., *Phys. Rev. B* **79**, 235333 (2009).
- [16] Hwang, E. H.; Adam, S., and Das Sarma, S., *Phys. Rev. Lett.* **98**, 186806 (2007).
- [17] Lemme, M. C.; Echtermeyer, T. J.; Baus, M., and Kurz, H., *IEEE Electr. Device L* **28**, 282-284 (2007).
- [18] Tan, Y. W.; Zhang, Y.; Bolotin, K.; Zhao, Y.; Adam, S.; Hwang, E. H.; Das Sarma, S.; Stormer, H. L., and Kim, P., *Phys. Rev. Lett.* **99**, 246803 (2007).
- [19] Zhang, Y. B.; Tan, Y. W.; Stormer, H. L., and Kim, P., *Nature* **438**, 201-204 (2005).
- [20] Novoselov, K. S.; McCann, E.; Morozov, S. V.; Fal'ko, V. I.; Katsnelson, M. I.; Zeitler, U.; Jiang, D.; Schedin, F., and Geim, A. K., *Nat. Phys.* **2**, 177-180 (2006).
- [21] Novoselov, K. S.; Jiang, Z.; Zhang, Y.; Morozov, S.V.; Stormer, H.L.; Zeitler, U.; Maan, J.C.; Boebinger, G.S.; Kim, P., and Geim, A.K., *Science* **315**, 1379-1379 (2007).
- [22] Lin, Y. M.; Dimitrakopoulos, C.; Jenkins, K. A.; Farmer, D. B.; Chiu, H. Y.; Grill, A., and Avouris, P., *Science* **327**, 662-662 (2010).
- [23] Liao, L.; Lin, Y. C.; Bao, M. Q.; Cheng, R.; Bai, J. W.; Liu, Y. A.; Qu, Y. Q.; Wang, K. L.; Huang, Y., and Duan, X. F., *Nature* **467**, 305-308 (2010).

- [24] Wu, Y. Q.; Lin, Y. M.; Bol, A. A.; Jenkins, K. A.; Xia, F. N.; Farmer, D. B.; Zhu, Y., and Avouris, P., *Nature* **472**, 74-78 (2011).
- [25] Fujita, M.; Wakabayashi, K.; Nakada, K., and Kusakabe, K., *J. Phys. Soc. Jpn.* **65**, 1920-1923 (1996).
- [26] Barone, V.; Hod, O., and Scuseria, G. E., *Nano Lett.* **6**, 2748-2754 (2006).
- [27] Yang, L.; Park, C. H.; Son, Y. W.; Cohen, M. L., and Louie, S. G., *Phys. Rev. Lett.* **99**, 186801 (2007).
- [28] K. R. Ratinac, W. R. Yang, S. P. Ringer, F. Braet, *Environ. Sci. Technol.*, **44**, 1167.
- [29] P. Hu, J. Zhang, L. Li, Z. Wang, W. O'Neill, P. Estrela, *Sensors*, **10**, 5133.
- [30] P. K. Ang, W. Chen, A. T. S. Wee, K. P. Loh, *J. Am. Chem. Soc.* **2008**, **130**, 14392.
"Solution-Gated Epitaxial Graphene as pH Sensor"
- [31] F. Chen, J. Xia, D. K. Ferry, N. Tao, *Nano Lett.* **2009**, **9**, 2571. "Dielectric Screening Enhanced Performance in Graphene FET"
- [32] F. Chen, Q. Qing, J. Xia, J. Li, N. Tao, *J. Am. Chem. Soc.* **2009**, **131**, 9908.
"Electrochemical Gate-Controlled Charge Transport in Graphene in Ionic Liquid and Aqueous Solution"
- [33] Y. Ohno, K. Maehashi, Y. Yamashiro, K. Matsumoto, *Nano Lett.* **2009**, **9**, 3318.
"Electrolyte-Gated Graphene Field-Effect Transistors for Detecting pH Protein Adsorption"
- [34] Z. Cheng, Q. Li, Z. Li, Q. Zhou, Y. Fang, *Nano Lett.* **2010**, **10**, 1864. "Suspended Graphene Sensors with Improved Signal and Reduced Noise"

- [35] Q. He, H. G. Sudibya, Z. Yin, S. Wu, H. Li, F. Boey, W. Huang, P. Chen, H. Zhang, *ACS Nano* **2010**, *4*, 3201. "Centimeter-Long and Large-Scale Micropatterns of Reduced Graphene Oxide Films: Fabrication and Sensing Applications"
- [36] X. Dong, Y. Shi, W. Huang, P. Chen, L.-J. Li, *Adv. Mater.* **2010**, *22*, 1649. "Electrical Detection of DNA Hybridization with Single-Base Specificity Using Transistors Based on CVD-Grown Graphene Sheets"
- [37] Park, S. and Ruoff, R. S., *Nat. Nanotechnol.* **4**, 217-224 (2009).
- [38] Li, X. S.; Cai, W. W.; An, J. H.; Kim, S.; Nah, J.; Yang, D. X.; Piner, R.; Velamakanni, A.; Jung, I.; Tutuc, E.; Banerjee, S. K.; Colombo, L., and Ruoff, R.S., *Science* **324**, 1312-1314 (2009).
- [39] Reina, A.; Jia, X. T.; Ho, J.; Nezich, D.; Son, H. B.; Bulovic, V.; Dresselhaus, M. S., and Kong, J., *Nano Lett.* **9**, 30-35 (2009).
- [40] Hawker, C. J. and Russell, T. P., *MRS Bull.* **30**, 952-966 (2005).
- [41] Xu, T.; Kim, H. C.; DeRouchey, J.; Seney, C.; Levesque, C.; Martin, P.; Stafford, C. M., and Russell, T. P., *Polymer* **42**, 9091-9095 (2001).
- [42] Cheng, J. Y.; Mayes, A. M., and Ross, C. A., *Nat. Mater.* **3**, 823-828 (2004).
- [43] Park, S.; Lee, D. H.; Xu, J.; Kim, B.; Hong, S. W.; Jeong, U.; Xu, T., and Russell, T. P., *Science* **323**, 1030-1033 (2009).
- [44] Bai, J. W.; Duan, X. F., and Huang, Y., *Nano Lett.* **9**, 2083-2087 (2009).
- [45] Sols, F.; Guinea, F., and Neto, A. H. C., *Phys. Rev. Lett.* **99**, 166803 (2007).
- [46] Li, T. C. and Lu, S. P., *Phys. Rev. B* **77**, 085408 (2008).
- [47] Wang, Joseph; *Chem. Rev.* **2008**, *108*, 814-825
- [48] Heller, A.; Feldman, Ben. *Chem. Rev.* **2008**, *108*, 2482–2505

- [49] Xiao, Y.; Patolsky, F.; Katz, E.; Hainfeld, J. F.; Willner, I. *Science* **2003**, *299*, 1877.
- [50] Song, Y.; Qu, K.; Zhao, C.; Ren, J.; Qu, X. *Adv. Mater.* **2010**, *22*, 1–5
- [51] Updike, S.; Hicks, G. *Nature* **1967**, *214*, 986.
- [52] Chenxin Cai and Jing Chen, *Analytical Biochemistry* **2004**, *332*, 75–83
- [53] Shan, C.; Yang, H.; Song, J.; Han, D.; Ivaska, A.; Niu, Li. *Anal. Chem.* **2009**, *81*, 2378–2382
- [54] Bartlett, P. N.; Birkin, P. R. *Anal. Chem.* **1994**, *66*, 1552.
- [55] Shul'ga, A. A.; Koudelka-Hep, M.; de Rooij, N. F. *Anal. Chem.* **1994**, *66*, 205-210
- [56] Forzani, E. S.; Zhang, H. Q.; Nagahara, L.; Amlani, I.; Tsue, R.; Tao, N. J. *Nano Lett.* **2004**, *4*, 1785.
- [57] Besteman, K.; Lee, F.; Wiertz, F.; Heering, H.; Dekker, C. *Nano Lett.* **2003**, *3*, 727.
- [58] Cella, L. N.; Chen, W.; Myung, N. V.; Mulchandani, A. *J. Am. Chem. Soc.* **2010**, *132*, 5024–5026
- [59] Garrido, J. A.; Nowy, S.; Hartl, A.; Stutzmann, M. *Langmuir* **2008**, *24*, 3897.
- [60] Lin, Y.; Lu, F.; Tu, Y.; Ren, Z. *Nano Lett.* **2004**, *4*, 191-195
- [61] Chen, Y. S.; Huang, J. H.; Chuang, C. C. *Carbon* **2009**, *47*, 3106–3112
- [62] Qu, Y.; Porter, R.; Shan, F.; Carter, J. D.; Guo, T. *Langmuir* **2006**, *22*, 6367-6374
- [63] Chen, F.; Qing, Q.; Xia, J.; Li, J.; Tao, N. *J. Am. Chem. Soc.* **2009**, *131*, 9908–9909
- [64] Heller, D. A.; Jin, H.; Martinez, B. M.; Patel, D.; Miller, B. M.; Yeung, T. K.; Jena, P. V.; Hobartner, C.; Ha, T.; Silverman, S. K.; Strano, M. S. *Nat.Nanotech.* **2009**, *4*, 114.
- [65] Ir.P.Bergveld Em. IEEE Sensor Conference Toronto, October 2003
- [66] Radomski, M.W. *et al.*, An L-arginine nitric-oxide pathway present in human

- platelets regulates aggregation. *Proc. Natl. Acad. Sci. U.S.A.* **87** (13), 5193-5197 (1990).
- [67] Langrehr, J.M. *et al.*, Nitric-oxide – a new endogenous immunomodulator. *Transplantation* **55** (6), 1205-1212 (1993).
- [68] Ignarro, L.J. *et al.*, Endothelium-derived relaxing factor produced and released from artery and vein is nitric-oxide. *Proc. Natl. Acad. Sci. U.S.A.* **84** (24), 9265-9269 (1987).
- [69] Ohta, A. *et al.*, Localization of nitric-oxide synthase-immunoreactive neurons in the solitary nucleus and ventrolateral medulla-oblongata of the rat – their relation to catecholaminergic neurons. *Neuroscience Letters* **158** (1), 33-35 (1993).
- [70] Hall, C. N. & Garthwaite, J., What is the real physiological NO concentration in vivo? *Nitric Oxide* **21**, 92–103 (2009).
- [71] Gryglewski, R.J., Palmer, R.M.J., & Moncada, S., Superoxide anion is involved in the breakdown of endothelium-derived vascular relaxing factor. *Nature* **320** (6061), 454-456 (1986).
- [72] Bedioui, F. & Villeneuve, N., Electrochemical nitric oxide sensors for biological samples - Principle, selected examples and applications. *Electroanalysis* **15** (1), 5-18 (2003).
- [73] Kim, J.H. *et al.*, The rational design of nitric oxide selectivity in single-walled carbon nanotube near-infrared fluorescence sensors for biological detection. *Nature Chem.* **1** (6), 473-481 (2009).
- [74] Kojima, H. *et al.*, Detection and imaging of nitric oxide with novel fluorescent indicators: diaminofluoresceins. *Anal. Chem.* **70**, 2446-2453 (1998).
- [75] Wardman, P. *et al.*, Fluorescent and luminescent probes for measurement of oxidative and nitrosative species in cells and tissues: Progress, pitfalls, and prospects.

Free Radical Biology & Medicine **43**, 995–1022 (2007).

[76] Bedioui, F. *et al.*, Elaboration and use of nickel planar macrocyclic complex-based sensors for the direct electrochemical measurement of nitric oxide in biological media. *Biosensors & Bioelectronics* **12** (3), 205-212 (1997).

[77] Lee, Y., Oh, B.K., & Meyerhoff, M.E., Improved planar amperometric nitric oxide sensor based on platinized platinum anode. 1. Experimental results and theory when applied for monitoring NO release from diazeniumdiolate-doped polymeric films. *Anal. Chem.* **76** (3), 536-544 (2004).

[78] Davies, I.R. & Zhang, X.J., Nitric oxide selective electrodes. *Methods in Enzymology* **436** (1), 63-95 (2008).

[79] Privett, B.J., Shin, J.H. & Schoenfish, M.H., Electrochemical nitric oxide sensors for physiological measurements. *Chem. Soc. Rev.* **39** (6), 1925-1935 (2010).

[80] Wu, D.G. *et al.*, Direct detection of low-concentration NO in physiological solutions by a new GaAs-based sensor. *Chemistry-a European Journal* **7** (8), 1743-1749 (2001).

[81] Zheng, G.F. *et al.*, Multiplexed electrical detection of cancer markers with nanowire sensor arrays. *Nature Biotechnology* **23** (10), 1294-1301 (2005).

[82] Chen, R.J. *et al.*, An investigation of the mechanisms of electronic sensing of protein adsorption on carbon nanotube devices. *J. Amer. Chem. Soc.* **126** (5), 1563-1568 (2004).

[83] Xue, T. *et al.*, Graphene-supported hemin as a highly active biomimetic oxidation catalyst. *Angew.Chem. Intl. Ed.* **51**, 3822-3825 (2012).

[84] Cooper, C.E., Nitric oxide and iron proteins. *Biochimica Et Biophysica Acta-Bioenergetics* **1411** (2-3), 290-309 (1999).

[85] Xu, Y. *et al.*, Chemically converted graphene induced molecular flattening of

- 5,10,15,20-tetrakis(1-methyl-4-pyridinio)porphyrin and its application for optical detection of cadmium(II) ions. *J. Amer. Chem. Soc.* **131** (37), 13490-13497 (2009).
- [86] Ferrari, A.C. Raman spectroscopy of graphene and graphite: disorder, electron-phonon coupling, doping and nonadiabatic effects. *Solid State Communications* **143** (1-2), 47-57 (2007).
- [87] Turner, J. *et al.*, Resonance Raman spectroscopy of oxoiron(IV) porphyrin π -cation radical and oxoiron(IV) hemes in peroxidase intermediates. *Journal of Inorganic Biochemistry* **100** (4), 480-501 (2006).
- [88] Rao, C.N.R. & Voggu, R., Charge-transfer with graphene and nanotubes. *Materials Today* **13** (9), 34-40 (2010).
- [89] Maragos, C.M. *et al.*, Complexes of NO with nucleophiles as agents for the controlled biological release of nitric-oxide – vasorelaxant effects. *Journal of Medicinal Chemistry* **34** (11), 3242-3247 (1991).
- [90] Hrabie, J. A. & John, R. K., New nitric oxide-releasing zwitterions derived from polyamines. *J. Org. Chem.* **58**, 1472-1476 (1993).
- [91] Keefer, L. K. *et al.*, NONOates" (1-Substituted Diazen- 1-ium- 1,2- diolates) as nitric oxide donors: convenient nitric oxide dosage forms. *Methods in Enzymology* **268**, 281-293 (1996).
- [92] Caraiman, D. *et al.*, The gas-phase chemistry of iron cations coordinated to benzene and the extended aromatic coronene. *International Journal of Mass Spectrometry* **223** (1-3), 411-425 (2003).
- [93] Hieringer, W. *et al.*, The surface trans effect: Influence of axial ligands on the surface chemical bonds of adsorbed metalloporphyrins. *J. Amer. Chem. Soc.* **133** (16), 6206-6222

(2011).

[94] Stuehr, D.J. & Marletta, M.A., Mammalian nitrate biosynthesis: Mouse macrophages produce nitrite and nitrate in response to Escherichia coli lipopolysaccharide. *Proc. Natl. Acad. Sci. U.S.A.* **82** (22), 7738-7742 (1985).

[95] Cha, W. *et al.*, Patterned electrode-based amperometric gas sensor for direct nitric oxide detection within microfluidic devices. *Anal. Chem.* **82** (8), 3300–3305 (2010).

[96] Pekarova, M. *et al.*, Continuous electrochemical monitoring of nitric oxide production in murine macrophage cell line RAW 264.7 *Analytical and Bioanalytical Chemistry* **394** (5), 1497–1504 (2009).

[97] Amatore, C. *et al.*, Monitoring in real time with a microelectrode the release of reactive oxygen and nitrogen species by a single macrophage stimulated by its membrane mechanical depolarization. *ChemBioChem* **7** (4), 653-661 (2006).

[98] Palmer, R. M. J. *et al.*, Vascular endothelial cells synthesize nitric oxide from L-arginine. *Nature* **333** (6174), 664-666 (1988).

[99] Malinski, T. & Taha, Z., Nitric oxide release from a single cell measured in situ by a porphyrinic-based microsensor. *Nature* **358** (6388), 676-678 (1992).

[100] Pailleret, A. *et al.*, In situ formation and scanning electrochemical microscopy assisted positioning of NO-sensors above human umbilical vein endothelial cells for the detection of nitric oxide release. *Electrochem. Commun.* **5**, 847-852 (2003).

[101] Clevenger, W. L., Smith, B. W. & Winefordner, J. D. Trace Determination of Mercury: A Review, *Critical Reviews in Analytical Chemistry*, **27**(1), 1-26 (1997).

[102] Leopold, K., Foulkes, M. & Worsfold, P. Methods for the determination and speciation of mercury in natural waters-A review. *Analytica Chimica Acta* **663**, 127-138

(2010).

[103] Chen, K. *et al.* Hg(II) Ion Detection Using Thermally Reduced Graphene Oxide Decorated with Functionalized Gold Nanoparticles. *Analytical Chemistry* **84**, 4057-4062 (2012).

[104] Yang, Y.K., Yook, K.J. & Tae, J. A rhodamine-based fluorescent and colorimetric chemodosimeter for the rapid detection of Hg²⁺ ions in aqueous media. *Journal of the American Chemical Society* **127**, 16760-16761 (2005).

[105] Lee, J.S., Han, M.S. & Mirkin, C.A. Colorimetric detection of mercuric ion (Hg²⁺) in aqueous media using DNA-functionalized gold nanoparticles. *Angewandte Chemie-International Edition* **46**, 4093-4096 (2007).

[106] Kawasaki, H., Hamaguchi, K., Osaka, I. & Arakawa, R. pH-Dependent Synthesis of Pepsin-Mediated Gold Nanoclusters with Blue Green and Red Fluorescent Emission. *Advanced Functional Materials* **21**, 3508-3515 (2011).

[107] Darbha, G.K., Ray, A. & Ray, P.C. Gold nanoparticle-based miniaturized nanomaterial surface energy transfer probe for rapid and ultrasensitive detection of mercury in soil, water, and fish. *Acs Nano* **1**, 208-214 (2007).

[108] Cho, E.S. *et al.* Ultrasensitive detection of toxic cations through changes in the tunnelling current across films of striped nanoparticles. *Nature Materials* **11**, 978-985 (2012).

[109] Knopfmacher, O. *et al.* Highly stable organic polymer field-effect transistor sensor for selective detection in the marine environment. *Nature Communications* **5**, 2954-2954 (2014).

[110] Mak, K. F., Lee, C., Hone, J., Shan, J. & Heinz, T. F. Atomically Thin MoS₂: A new

- direct-gap semiconductor. *Phys. Rev. Lett.* **105**, 136805 (2010).
- [111] Wang, Q. H., Kalantar-Zadeh, K., Kis, A., Coleman, J. N. & Strano, M. S. Electronics and optoelectronics of two-dimensional transition metal dichalcogenides. *Nat. Nanotechnol.* **7**, 699-712 (2012).
- [112] He, Q.Y. *et al.* in *Small*, Vol. 8 2994-2999 (2012).
- [113] Late, D.J. *et al.* Sensing Behavior of Atomically Thin-Layered MoS₂ Transistors. *Acs Nano* **7**, 4879-4891 (2013).
- [114] Lee, K., Gatensby, R., McEvoy, N., Hallam, T. & Duesberg, G.S. High-Performance Sensors Based on Molybdenum Disulfide Thin Films. *Advanced Materials* **25**, 6699-6702 (2013).
- [115] Li, H. *et al.* Fabrication of Single- and Multilayer MoS₂ Film-Based Field-Effect Transistors for Sensing NO at Room Temperature. *Small* **8**, 63-67 (2012).
- [116] Perkins, F.K. *et al.* Chemical Vapor Sensing with Mono layer MoS₂. *Nano Letters* **13**, 668-673 (2013).
- [117] Mouri, S., Miyauchi, Y., & Matsuda, K. Tunable Photoluminescence of Monolayer MoS₂ via Chemical Doping, *Nano Letters* **13**, 5944–5948 (2013).
- [118] Korn, T. *et al.* Low-temperature photocarrier dynamics in monolayer MoS₂, *Applied Physics Letters* **99**, 102109 (2011).